THESIS FOR THE DEGREE OF LICENTIATE OF ENGINEERING

# Test Methodologies for Large Cylindrical Battery Cells in Heterogeneous Conditions

Daniel Poposki

Department of Electrical Engineering
Chalmers University of Technology
Gothenburg, Sweden, 2026

**Test Methodologies for Large Cylindrical Battery Cells in Heterogeneous Conditions**

Daniel Poposki



Department of Electrical Engineering
Chalmers University of Technology
SE-412 96 Gothenburg, Sweden
Phone: +46 (0)31 772 1000

Printed by Chalmers Digital Printing
Gothenburg, Sweden, September 2026

# Abstract

This thesis develops and evaluates experimental methods for studying electrochemical and thermal nonuniformity in lithium ion cells. Laboratory cell with varying SiOx content in the graphite electrode (Si–Gr) were used to investigate voltage signatures and the influence of state of charge on ageing. Prototype 4695 cylindrical cells were studied under different current, temperature, and cooling conditions. The methods included slow cycle voltage analysis, capacity measurements, intermittent current interruption, reconstruction of the galvanostatic state of charge window, surface temperature measurements, and computed tomography.

For the laboratory cells, C/20 voltage hysteresis increased systematically with nominal $SiO_x$ content and showed the clearest separation at low state of charge. The 4695 cell showed the closest agreement with the nominal 10% $SiO_x$ reference, although its exact silicon content could not be determined. The 15% Si–Gr cells cycled over 0–50% state of charge reached approximately 80% state of health (SoH) after 290 equivalent full cycles, compared with about 350 equivalent full cycles for the 0–100% window.

The 4695 cells showed both gradual capacity fade and pronounced knee behaviour in the SoH trajectory. The End of Life (EoL) criteria at 80% SoH ranged from approximately 350 to 1030 equivalent full cycles, with differences of approximately 150–250 equivalent full cycles between nominal replicate cells. The accessible SoC window generally contracted through a downward shift of the upper boundary. Resistance growth, window contraction, and accelerated capacity fade occurred together in several cells, but no universal relation was identified.

The partial cooling system imposed average axial surface temperature gradients of approximately 5–8 °C, with peak differences up to approximately 13 °C. The results demonstrate the methodology but do not establish that the imposed gradient alone caused the observed degradation. Computed tomography also revealed apparent core collapse in one aged cell.

Overall, the work shows that capacity, resistance, accessible state of charge window, temperature distribution, and structural observations provide complementary information. The developed methods form a basis for further studies using more mature cells, improved contact and sensor control, larger sample groups, and systematic teardown analysis.

**Keywords:** Li-ion, Battery, Heterogeneous, Ageing, Cylindrical, Cell, 4695

## Acknowledgments

This work was carried out within the HALIBatt project, funded by the Swedish Electromobility Centre (SEC) and supported by Volvo Technology. I would like to sincerely thank my supervisors at Chalmers University of Technology and Volvo for their guidance, encouragement, and valuable discussions throughout this work. I am also grateful to all HALIBatt project members and collaborators at Chalmers, KTH Royal Institute of Technology, Uppsala University, Scania, Volvo Cars, and the other participating organisations for their scientific contributions and cooperation. Finally, I would like to thank my colleagues, friends, and family for their encouragement and support throughout this journey.

# Acronyms

| | |
|---|---|
| AG: | Artificial Graphite |
| BoL: | Beginning of Life |
| CC: | Constant Current |
| CL: | Contact Loss |
| CT: | Computed Tomography |
| CV: | Constant Voltage |
| DVA: | Differential Voltage Analysis |
| EoL: | End of Life |
| ICA: | Incremental Capacity Analysis |
| ICI: | Intermittent Current Interruption |
| LAM: | Loss of Active Material |
| LLI: | Loss of Lithium Inventory |
| MoL: | Middle of Life |
| NCA: | Lithium Nickel Cobalt Aluminium Oxide |
| NMC: | Lithium Nickel Manganese Cobalt Oxide |
| OCV: | Open Circuit Voltage |
| RPT: | Reference Performance Test |
| SEI: | Solid Electrolyte Interphase |
| Si–Gr: | Silicon–Graphite |
| $SiO_x$: | Silicon Oxide |
| SoC: | State of Charge |
| SoH: | State of Health |

# Contents

**Abstract** i

**Acknowledgements** iii

**Acronyms** iv

**1 Introduction** 1
- 1.1 Background . . . 1
- 1.2 Previous Work . . . 2
- 1.3 Purpose . . . 3
- 1.4 Contributions . . . 4
- 1.5 Thesis Outline . . . 4

**2 Theory** 7
- 2.1 Lithium-ion Batteries . . . 7
  - Electrochemical Reactions . . . 8
  - Electrode Materials . . . 10
  - Cell Formats . . . 12
  - State of Charge, Polarization and Hysteresis . . . 13
- 2.2 Ageing in lithium-ion batteries . . . 15
  - SEI Growth and Loss of Lithium Inventory . . . 16

SEI Decomposition and Precipitation . . . . . 16
Solvent co-intercalation and Graphite Exfoliation . . . . . 16
Lithium Plating and Dendrite Formation . . . . . 17
Loss of Active Material . . . . . 17
Binder Degradation and Contact Loss . . . . . 18
Current Collector Degradation . . . . . 18
Positive Electrode and Electrolyte Degradation . . . . . 19
Internal Short Circuit . . . . . 19
Influence of Operating Conditions . . . . . 20
Heterogeneous Ageing . . . . . 20
2.3 In-situ Characterisation Techniques . . . . . 21
Capacity and resistance measurements . . . . . 21
Differential Voltage and Incremental Capacity Analysis . . . . . 21
Intermittent Current Interruption . . . . . 22
Computed Tomography . . . . . 23

**3 Experimental Setups and Methodologies** **25**
3.1 Test Equipment . . . . . 25
3.2 Test Objects . . . . . 26
3.3 Ageing Test Matrix for 4695 Format Cells . . . . . 26
3.4 Test Protocol . . . . . 27
3.5 Cooling System for Temperature Gradients . . . . . 28
3.6 Silicon-Graphite Composite Cells . . . . . 30

**4 Electrochemical Signatures of Cells Containing $SiO_x$** **35**
4.1 Beginning of Life Electrochemical Signatures . . . . . 35
Voltage Curves and Hysteresis as a Function of $SiO_x$ Content . 35
4.2 Ageing in Different State of Charge Windows . . . . . 39
Evolution of Electrochemical Signatures During Ageing . . . . 41

**5 Ageing of Cylindrical 4695-format Cells** **43**
5.1 Test Matrix Overview . . . . . 43
5.2 Cell Capacity . . . . . 44
5.3 Evolution of the Galvanostatic Cycling SoC Window . . . . . 49
5.4 ICI Resistance in Relation to the SoC Window . . . . . 55
5.5 Thermal Profiles . . . . . 61
5.6 CT Observations of Internal Structural . . . . . 67

**6 Conclusions and Future Work** **71**
6.1 Future Work . . . . . 73

**References** **75**

# CHAPTER 1

# Introduction

This chapter introduces the motivation and context for the thesis. It summarises the background and relevant previous work as well as states the purpose and main contributions of this thesis.

## 1.1 Background

Electrification of road transport is accelerating in Sweden, driven by the need to reduce greenhouse gas emissions and decrease dependence on fossil fuels. This transition is shaped by the national climate policy framework, which sets a long-term target of net-zero greenhouse gas emissions by 2045 [1]. The Swedish Electromobility Centre highlights the role of coordinated research and industry collaboration in supporting transport electrification [2].

Lithium-ion batteries are commonly used as the energy storage technology for electric vehicles, due to their performance characteristics. Battery ageing directly impacts vehicle range, lifetime, and cost. While improvements in cell chemistry, design, and manufacturing have extended durability, degradation rarely distributes uniformly across large format cells. Hence in most applications, large format cells rarely operate under uniform conditions. Spatial

variations in temperature and current distribution arise from geometry, tab and electrode design, manufacturing tolerances, and non-uniform cooling and mechanical interfaces at a system level. Under high power operation, these gradients become larger, which can cause heterogeneous degradation patterns.

Localised degradation phenomena such as lithium plating and loss of active material may develop and accelerate in specific regions [3], [4]. Recent studies indicate that even small thermal gradients can significantly alter ageing trajectories and degradation modes, motivating explicit consideration of heterogeneity in test design [5]. System level analyses of next generation large cylindrical formats further emphasise that scaling increases electro-thermal non-uniformity and that new measurement methodologies are required to quantify gradients under realistic boundary conditions [6].

These heterogeneous effects create practical challenges for large format cells. For battery pack integration, it is often insufficient to specify only an operating temperature range or a maximum allowable temperature. Non-uniform boundary conditions can produce significant temperature gradients within the cell, which may alter current distribution and accelerate local degradation. Therefore, acceptable thermal gradients, as well as their measurement definition, could be specified together with the cooling interface and validation test case. This thesis addresses this need by developing methodologies to evaluate performance and ageing relevant signatures under intentionally heterogeneous conditions.

## 1.2 Previous Work

Ageing in lithium-ion cells is strongly influenced by operating conditions such as temperature, charging rate, and state of charge window. Studies on large format cells demonstrate that different ageing mechanisms can dominate depending on severity and boundary conditions. Reported degradation modes include particle cracking, lithium plating, and gas evolution, with transitions between these regimes as C-rate and temperature change [7], [8]. Degradation has also been reported to differ between curved and flat regions of jelly roll electrodes, where adhesion loss in wound sections may accelerate ageing [9].

Lithium plating remains a central concern for fast charging and low temperature operation and has therefore been studied using combinations of electrochemical indicators and post-mortem validation [10]. Many modelling and

diagnostic approaches still rely on spatially lumped descriptions and therefore do not fully capture heterogeneity in large-format cells, limiting interpretability and predictive capability.

Despite advances, there remains a gap between insights from specialised studies and models, and repeatable, engineering-relevant test methodologies for large format cylindrical cells under heterogeneous thermal boundary conditions. In particular, the literature provides limited studies on experiments designed to generate controlled and directional temperature gradients and link observed cell level signatures. This thesis addresses this gap by developing and demonstrating an ageing test matrix and supporting diagnostic workflow for 4695 format cylindrical cells, including controlled partial cooling configurations to induce gradients.

## 1.3 Purpose

The purpose of this thesis is to improve the understanding of ageing in lithium-ion batteries by studying how non-uniform operating conditions influence degradation in large format cylindrical cells. The work focuses on experimental ageing studies of 4695 cells under controlled but intentionally heterogeneous boundary conditions, with particular emphasis on partial cooling configurations and their effect on cell ageing behaviour. More specifically, this thesis aims to:

- Investigate and implement a test setup jig that enables control of temperature gradients across the cell.
- Evaluate results of an ageing test matrix for 4695 cylindrical cells as a practical method for studying heterogeneous ageing under different cycling and cooling conditions.
- Investigate how partial cooling and other non-uniform boundary conditions influence capacity fade, resistance growth, thermal behaviour, and electrochemical signatures.
- Establish reference electrochemical signatures in Si–Gr laboratory cells to support interpretation of the behaviour observed in the commercial cells.

## 1.4 Contributions

This thesis contributes to the experimental study of ageing and heterogeneous ageing in large format cylindrical lithium ion cells. The main contributions are:

- **Test methodology for heterogeneous ageing of 4695 cells.** An ageing test matrix and a partial cooling system were developed and successfully demonstrated using prototype 4695 cells. The cooling system imposed controlled axial surface temperature gradients up to 8 °C during long term cycling.

- **Combined analysis of ageing in large cylindrical cells.** Capacity retention, galvanostatic SoC window evolution, ICI resistance, surface temperature profiles, and selected CT observations were evaluated together. The results demonstrate the value and limitations of combining several diagnostic quantities when interpreting ageing.

- **Reference measurements for Si–Gr cells.** Laboratory cells with controlled $SiO_x$ content were used to establish voltage hysteresis signatures and to investigate ageing in different SoC windows. These measurements provide controlled references for interpreting the electrochemical response of the 4695 cells.

## 1.5 Thesis Outline

The thesis is structured as follows:

- **Chapter 2** presents the theoretical background on lithium-ion cells, ageing mechanisms, heterogeneous ageing, and the characterisation methods used in this work.

- **Chapter 3** describes the test objects, equipment, cycling protocols, partial cooling system, and laboratory Si–Gr cell experiments.

- **Chapter 4** presents the electrochemical signatures of cells with different $SiO_x$ contents and their ageing in different SoC windows.

- **Chapter 5** presents the ageing results for the 4695-format cells, including capacity retention, SoC window evolution, ICI resistance, thermal profiles, and CT-scan observations.
- **Chapter 6** summarises the main conclusions, limitations, and recommendations for future work.

# CHAPTER 2

# Theory

## 2.1 Lithium-ion Batteries

Lithium-ion batteries store and release energy by the reversible transfer of lithium between two host electrodes. A lithium-ion battery cell consists of a positive electrode, a negative electrode, a porous separator, electrolyte, and two current collectors. The electrodes store lithium by insertion, intercalation, alloying, or conversion reactions depending on the electrode chemistry and structure. The electrolyte provides ionic conductivity between the electrodes, while the separator prevents direct electronic contact between them. The current collectors provide electronic connection between the porous electrodes and the external circuit.

During discharge, lithium is removed from the negative electrode and inserted into the positive electrode. Lithium ions, $Li^+$, migrate through the electrolyte filled separator, while electrons cannot pass through the separator and therefore travel through the external circuit. The electron flow through the external load delivers useful electrical work. During charge, an external power source drives the reverse process: $Li^+$ is extracted from the positive electrode and inserted into the negative electrode, while electrons are sup-

plied to the negative electrode through the external circuit. The cell voltage is determined by the difference in electrochemical potential between the two electrodes and varies with state of charge, temperature, current load, and ageing state [11], [12], [13].

Although the graphite side is commonly referred to as the anode and the positive electrode side the cathode in battery literature, these terms are strictly process dependent. The anode is the electrode where oxidation occurs and the cathode is the electrode where reduction occurs. Thus, during discharge the negative electrode is the anode and the positive electrode is the cathode, whereas during charging the electrochemical definitions are reversed. Figure 2.1 illustrates a schematic overview of the working principle and selected degradation mechanisms in a lithium-ion cell.

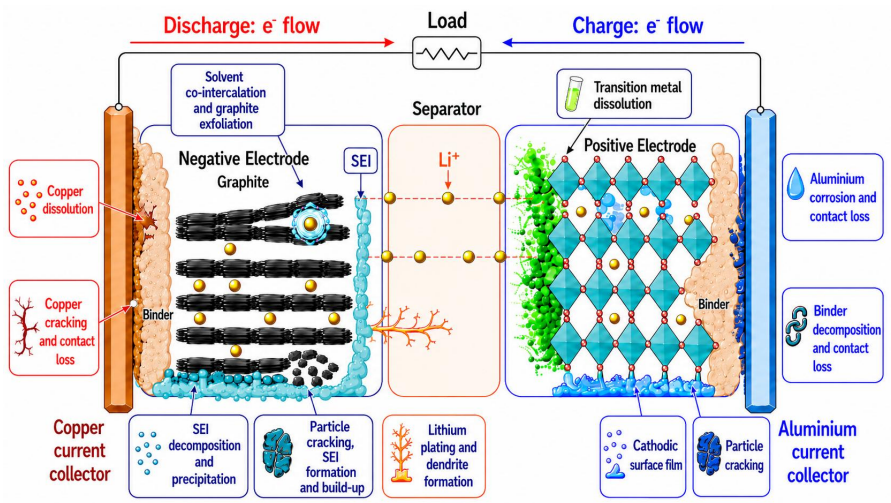


**Figure 2.1:** Schematic overview of the working principle and selected degradation mechanisms in a lithium-ion cell.

## Electrochemical Reactions

The operation and degradation of a lithium-ion cell are strongly coupled. During normal cycling, lithium ions must be transported through the electrolyte, across the electrode and electrolyte interfaces, and inside the active mate-

rial particles. At the same time, electrons must be transported through the active material, conductive additive, binder network, current collector, and external circuit. Any process that consumes cyclable lithium, isolates active material, or increases electronic or ionic resistance will therefore reduce cell performance.

The working principle of a lithium-ion cell can be described by coupled oxidation and reduction reactions at the two electrodes. For a graphite-based negative electrode and a layered transition-metal oxide positive electrode, the charge reactions may be written in simplified form as

$$\mathrm{LiMO_2} \rightarrow \mathrm{Li_{1-x}MO_2} + x\mathrm{Li^+} + x\mathrm{e^-} \tag{2.1}$$

$$\mathrm{C_6} + x\mathrm{Li^+} + x\mathrm{e^-} \rightarrow \mathrm{Li_xC_6} \tag{2.2}$$

Here, M represents the transition-metal framework of the positive electrode, for example Ni, Mn and Co in an NMC type layered oxide. During charge, lithium is extracted from the positive electrode and inserted into the negative electrode. The overall charging reaction can therefore be written as

$$\mathrm{C_6} + \mathrm{LiMO_2} \rightarrow \mathrm{Li_xC_6} + \mathrm{Li_{1-x}MO_2} \tag{2.3}$$

During discharge, the reaction proceeds in the opposite direction:

$$\mathrm{Li_xC_6} + \mathrm{Li_{1-x}MO_2} \rightarrow \mathrm{C_6} + \mathrm{LiMO_2} \tag{2.4}$$

For a Si–Gr composite negative electrode, part of the lithium is stored in graphite by intercalation, while a part can be stored in silicon-based domains by alloying. The graphite intercalation reaction may be written as

$$\mathrm{C_6} + x\mathrm{Li^+} + x\mathrm{e^-} \rightleftharpoons \mathrm{Li_xC_6} \tag{2.5}$$

whereas the silicon contribution can be represented schematically as

$$\mathrm{Si} + y\mathrm{Li^+} + y\mathrm{e^-} \rightleftharpoons \mathrm{Li_ySi} \tag{2.6}$$

This simplified notation represents lithium storage in silicon-based domains; in practical composite electrodes, the silicon-containing phase may be present as $\mathrm{SiO}_x$ and the lithiation process is more complex than the idealized reaction presented in (2.6). The high storage capacity of silicon based materials is one reason why Si–Gr composite electrodes can increase cell energy density.

However, the larger volume change associated with silicon lithiation also makes the negative electrode more susceptible to mechanical degradation, particle cracking, and renewed solid electrolyte interphase (SEI) formation.

The equilibrium cell voltage is related to the electrochemical potentials of the two electrodes and can be expressed as

$$E_{\text{cell}} = E_{\text{pos}} - E_{\text{neg}} \tag{2.7}$$

where $E_{\text{pos}}$ and $E_{\text{neg}}$ are the equilibrium potentials of the positive and negative electrodes, respectively. The electrical work is related to the Gibbs free energy change by

$$\Delta G = -nFE_{\text{cell}} \tag{2.8}$$

where $n$ is the number of electrons transferred and $F$ is Faraday's constant. This relation shows why a larger potential difference between the electrodes corresponds to a higher cell voltage and therefore higher energy per unit charge.

## Electrode Materials

Commercial automotive lithium-ion cells commonly use layered transition-metal oxides as positive electrode materials because they provide high energy density. Examples include lithium nickel manganese cobalt oxides, often abbreviated NMC, and lithium nickel cobalt aluminium oxides, abbreviated NCA. The negative electrode is most commonly based on graphite because graphite has good reversibility, a low operating potential versus $\text{Li}/\text{Li}^+$, and long cycle life. However, graphite has a limited theoretical specific capacity of approximately 372 mAh $\text{g}^{-1}$, corresponding to the formation of $\text{LiC}_6$ at full lithiation [13], [14].

To increase energy density, graphite is lately often blended with silicon based materials such as silicon or silicon oxide, here denoted $\text{SiO}_x$. Silicon based materials can store substantially more lithium per unit mass than graphite, but they also undergo much larger volume changes during lithiation and delithiation. In a Si–Gr composite electrode, graphite provides a mechanically and electrochemically stable host, while the silicon-containing fraction increases the electrode capacity. This makes Si–Gr electrodes attractive for high-energy cells, but it also introduces additional degradation pathways related to mechanical stress, cracking, renewed SEI formation, and voltage hysteresis [14], [15].

The addition of $SiO_x$ changes both the electrochemical and mechanical response of the negative electrode. The capacity contribution increases, but the electrode also becomes more sensitive to local state of charge, cycling depth, and mechanical degradation. Silicon-containing domains generally show larger volume expansion and more pronounced hysteresis than graphite. As a result, Si–Gr cells can have higher beginning-of-life energy density, but may also be more sensitive to operating conditions that repeatedly utilise the silicon-rich part of the electrode [14], [15]. Figure 2.2 illustrates a Si–Gr composite electrode.

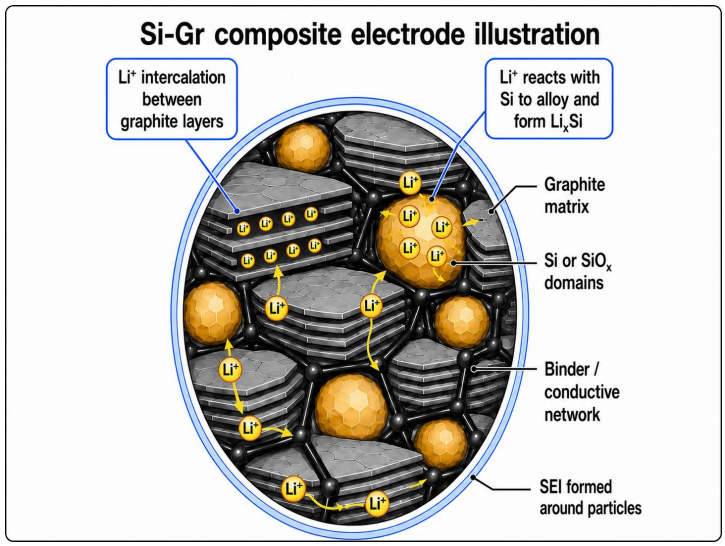


**Figure 2.2:** Conceptual illustration of a Si–Gr composite negative electrode. Graphite stores lithium mainly by intercalation between graphitic layers, while silicon based domains store lithium by alloying reactions. The silicon contribution increases the capacity of the negative electrode, but the larger volume changes of silicon based materials can accelerate mechanical degradation and SEI growth.

## Cell Formats

Lithium-ion cells are manufactured in several form factors, sizes, and geometries. The most common commercial formats are cylindrical, pouch, and prismatic cells. Although all formats are based on the same fundamental electrochemical principle, their mechanical construction, thermal behaviour, pack integration, and ageing characteristics can differ substantially.

Cylindrical cells consist of long coated electrode sheets and separators wound into a jelly-roll structure. The wound structure is inserted into a cylindrical metal can and connected to the cell terminals through tabs or tabless current-collector designs. Cylindrical cells are mechanically robust and benefit from a well-established manufacturing route. Small cylindrical cells, such as 18650 and 21700 formats, have been widely used in consumer electronics and electric vehicles. Larger cylindrical formats such as 4680 and 4695 cells, have received increased interest because they can reduce the number of cells, welds, interconnects, and monitoring channels required at pack level. This can reduce inactive material and simplify pack integration.

Pouch cells use stacked or folded electrode sheets enclosed in a flexible laminated pouch. This format provides high packaging efficiency and can achieve high gravimetric energy density because the casing mass is low. The flexible pouch also allows the cell to expand more easily during gas generation or electrode swelling. However, pouch cells generally require external mechanical support from the module or pack structure to maintain stack pressure and protect the cell from deformation. Their thermal and mechanical behaviour therefore depends strongly on how they are compressed, cooled, and integrated into the battery system.

Prismatic cells use a rigid rectangular casing, often made of aluminium or steel. The electrodes inside a prismatic cell may be stacked, wound, or arranged as a flattened jelly roll. Prismatic cells are attractive for pack integration because their rectangular geometry provides efficient space filling and relatively simple mechanical assembly. The rigid casing gives better mechanical protection than a pouch cell, but it also adds inactive mass. Large prismatic cells can have strong internal gradients because of their large dimensions and the distance between internal regions and cooled surfaces.

The choice of cell format affects the design of the battery system. Cylindrical cells are robust and modular, but their curved geometry leaves gaps between neighbouring cells unless additional potting, cooling, or structural ma-

terial is used. Pouch and prismatic cells can use pack volume more efficiently, but they place different requirements on compression, swelling management, and thermal interfaces. Therefore, cell format is not only a packaging choice; it also influences current distribution, heat management, mechanical stress, safety design, and ageing behaviour.

Increasing the size of a cylindrical cell can reduce the number of cells and inactive components at pack level, but it also increases the challenge of maintaining homogeneous internal conditions. Larger cylindrical cells are more prone to temperature gradients, non-uniform current density, and non-uniform mechanical stress within the jelly roll [6], [16], [17]. These gradients can affect both performance and ageing. For example, temperature gradients can lead to non-uniform reaction rates, while pressure and stress gradients can influence local porosity, transport resistance, and lithium plating tendency. Therefore, large-format cylindrical cells require careful thermal, mechanical, and electrochemical design.

In large cylindrical cells, the wound jelly roll creates different paths for heat to move through the cell. Heat can travel radially toward the side wall or axially toward the cell ends. Cooling may therefore be applied through the side wall, through one or both ends, or through a combination of these surfaces. The effectiveness of each approach depends on the thermal conductivity of the jelly roll, the current collector and tab design, and the thermal contact between the jelly roll and the cell casing. Consequently, cells with the same chemistry can show different temperatures, performance, and ageing behaviour depending on their design and cooling boundary conditions. These effects are important when interpreting heterogeneous ageing experiments on large format cells.

## State of Charge, Polarization and Hysteresis

State of charge, SoC, describes the amount of charge remaining in the cell relative to a defined full-cell capacity. If the current is defined as positive during discharge, the discharged capacity can be calculated as

$$Q(t) = \int_{t_0}^{t} I(\tau)\,\mathrm{d}\tau, \tag{2.9}$$

where $I$ is the applied current. When $I$ is given in ampere and time in seconds, the capacity in ampere-hours is obtained by

$$Q_{\mathrm{Ah}}(t) = \frac{1}{3600} \int_{t_0}^{t} I(\tau)\, \mathrm{d}\tau. \tag{2.10}$$

A practical definition of SoC during discharge is then

$$\mathrm{SoC}(t) = \frac{Q_{\max} - Q(t)}{Q_{\max} - Q_{\min}}, \tag{2.11}$$

where $Q_{\max}$ and $Q_{\min}$ define the usable capacity window. In ageing studies, the exact SoC definition must be stated carefully because the measured capacity changes as the cell ages.

The SoC is commonly related to the open circuit voltage, OCV, although the OCV–SoC relationship depends strongly on cell chemistry and is not generally linear. For a full cell, the measured OCV is the difference between the equilibrium potentials of the positive and negative electrodes.

When current is applied, the measured cell voltage differs from the equilibrium voltage due to polarization. This polarization includes ohmic losses in electronic and ionic pathways, charge-transfer losses at the electrode/electrolyte interfaces, and concentration losses associated with mass transport in the electrolyte and active-material particles. A simple expression for the terminal voltage during discharge is

$$V_{\mathrm{cell}} = E_{\mathrm{cell}} - \eta_{\mathrm{ohmic}} - \eta_{\mathrm{ct}} - \eta_{\mathrm{mt}}, \tag{2.12}$$

where $\eta_{\mathrm{ohmic}}$, $\eta_{\mathrm{ct}}$, and $\eta_{\mathrm{mt}}$ represent ohmic, charge-transfer, and mass-transport polarization, respectively. During charge, the sign of the polarization contribution is reversed relative to the equilibrium voltage. The increase in polarization during ageing is closely related to resistance and power fade [13], [18].

Charge-transfer kinetics at an electrode and electrolyte interface are commonly described by the Butler–Volmer equation

$$j = j_0 \left[ \exp\left( \frac{\alpha_{\mathrm{a}} F \eta}{RT} \right) - \exp\left( -\frac{\alpha_{\mathrm{c}} F \eta}{RT} \right) \right], \tag{2.13}$$

where $j$ is the interfacial current density, $j_0$ is the exchange current density, $\alpha_{\mathrm{a}}$ and $\alpha_{\mathrm{c}}$ are anodic and cathodic charge-transfer coefficients, $F$ is Faraday's

constant, $R$ is the gas constant, $T$ is temperature, and $\eta$ is the charge-transfer overpotential. This expression illustrates why reaction kinetics depend on temperature, local concentration, and overpotential.

Voltage hysteresis describes the difference between the charge and discharge voltage at the same SoC:

$$\Delta V_{\mathrm{hys}}(\mathrm{SoC}) = V_{\mathrm{ch}}(\mathrm{SoC}) - V_{\mathrm{dis}}(\mathrm{SoC}). \tag{2.14}$$

In graphite-only cells, the hysteresis is often moderate. In cells with silicon-containing negative electrodes, the hysteresis can be more pronounced due to the alloying behaviour and mechanical response of the silicon based component [13], [14].

## 2.2 Ageing in lithium-ion batteries

Ageing in lithium-ion batteries can be observed as capacity fade and resistance increase. Capacity fade reduces the amount of charge and energy that can be stored or delivered by the cell. Resistance increase reduces power capability and increases heat generation during operation. Together, these changes are commonly used to describe the state of health of a cell [12], [13], [19].

Battery ageing is caused by several coupled physical and chemical processes that occur in parallel. It is useful to distinguish between degradation mechanisms and degradation modes. Degradation mechanisms are the underlying reactions or physical processes, such as SEI growth, lithium plating, particle cracking, electrolyte oxidation, or current collector corrosion. Degradation modes describe the measurable cell-level consequences of these mechanisms. Common degradation modes are loss of lithium inventory (LLI), loss of active material (LAM), and contact or conductivity loss (CL) [11], [20].

LLI refers to the loss of cyclable lithium from the main reversible cell reaction. This can occur through SEI growth, lithium plating, electrolyte decomposition, or other parasitic side reactions that bind lithium in inactive products. LAM refers to the loss or isolation of active electrode material, so that part of the positive or negative electrode can no longer participate reversibly in lithium storage. CL refers to a loss of electronic or ionic pathways, for example through binder degradation, current collector corrosion, electrode cracking, or loss of interfacial contact.

## SEI Growth and Loss of Lithium Inventory

At the low potential of the negative electrode, the electrolyte is thermodynamically unstable and is partially reduced. The reduction products form a passivating surface layer known as the solid electrolyte interphase, SEI. A stable SEI is necessary for long-term cell operation because it limits continuous electrolyte reduction while still allowing lithium-ion transport. However, SEI formation consumes cyclable lithium and electrolyte. Continued SEI growth during ageing therefore leads to LLI and capacity fade. The SEI also adds transport resistance at the particle to electrolyte interface and can contribute to impedance rise [12], [13].

SEI growth is especially important in cells with silicon-containing negative electrodes. Silicon based particles expand and contract more than graphite during cycling. This repeated mechanical breathing can crack particles or surface films, expose fresh electrode surface, and promote renewed electrolyte reduction. As a result, SEI growth and mechanical degradation are strongly coupled in Si–Gr electrodes [14], [15].

## SEI Decomposition and Precipitation

The SEI is not a fixed layer. Its composition, thickness, and morphology evolve during cycling and storage. Decomposition products from the electrolyte or existing SEI can precipitate on electrode surfaces or inside pores. Such deposits may thicken surface films, reduce active surface area, clog pores, and increase ionic transport resistance. In Figure 2.1, SEI decomposition and precipitation are therefore shown as separate from simple SEI formation, although both contribute to the same broader degradation modes, LLI and impedance increase.

## Solvent co-intercalation and Graphite Exfoliation

Graphite stores lithium mainly by intercalation between graphitic layers. Under normal conditions, lithium ions shed most of their solvation shell before entering the graphite galleries. Under unfavourable conditions, solvated lithium species can co-intercalate into graphite. In this case, lithium enters together with solvent molecules or part of its solvent shell. This can expand the spacing between graphite layers and mechanically damage the graphite structure, leading to graphite exfoliation [12].

Graphite exfoliation reduces the structural integrity of the negative electrode. It can isolate parts of the graphite from the conductive network, create fresh surface area for further SEI formation, and increase the cell resistance. Thus, solvent co-intercalation and exfoliation can contribute to LAM, LLI, and CL simultaneously.

### Lithium Plating and Dendrite Formation

Lithium plating occurs when lithium ions are reduced to metallic lithium on the negative electrode surface instead of being inserted into graphite or the Si–Gr host. This can occur when the local negative-electrode potential falls to 0 V versus $Li/Li^+$. Conditions that promote this include fast charging, low temperature, high SoC, high local current density, transport limitations, and non-uniform internal pressure or temperature [16], [21], [22].

Plated lithium may be partly reversible if it is stripped during later discharge or re-intercalates during relaxation. However, irreversible lithium plating consumes cyclable lithium and therefore causes LLI. Metallic lithium also reacts with the electrolyte and forms additional SEI-like products, increasing both lithium loss and impedance. In severe cases, lithium deposits can form mossy or dendritic structures. If such structures penetrate or damage the separator and create an electronic connection between the electrodes, an internal short circuit can occur [21], [22].

In large cylindrical cells, the risk of lithium plating is not determined only by the applied current and ambient temperature. Local stress, electrolyte distribution, current density, and temperature can vary along the jelly roll. These local conditions can make plating more likely in selected regions, even when the global cycling condition appears acceptable [16].

### Loss of Active Material

Loss of active material means that part of the electrode can no longer participate reversibly in lithium storage. This can occur if active material particles crack, lose electrical contact, become blocked by surface films, or undergo structural changes that reduce their reversible capacity.

Particle cracking is driven by mechanical stress during lithiation and delithiation. Concentration gradients inside particles create spatially varying strain, while repeated expansion and contraction fatigue the particle and electrode

structure. In Si–Gr electrodes, this process is particularly important because the silicon-containing fraction undergoes much larger volume changes than graphite [14], [15]. Cracking can electrically isolate active material, leading to LAM. It also exposes fresh surfaces to the electrolyte, causing renewed SEI formation and additional LLI.

Particle cracking can also occur in positive electrode materials. Positive electrode cracking can expose reactive surfaces, promote electrolyte oxidation, accelerate surface-film formation, and facilitate transition-metal dissolution. Thus, cracking in either electrode can contribute to capacity fade, impedance rise, and heterogeneous ageing [12], [13].

### Binder Degradation and Contact Loss

The porous electrode coating is a composite of active material, conductive additive, binder, and pores filled with electrolyte. The binder maintains mechanical cohesion and adhesion to the current collector, while the conductive network provides electronic pathways between active particles and the current collector. During ageing, binder decomposition, electrode swelling, repeated mechanical strain, gas formation, or particle cracking can damage this network.

When particles lose contact with the conductive network, they may become partly or completely inactive. This increases resistance and can also appear as loss of active material at the full-cell level. Binder degradation and contact loss are therefore important contributors to CL and can indirectly contribute to LAM.

### Current Collector Degradation

The negative electrode is typically coated on a copper current collector because copper is relatively stable at the low potentials of the negative electrode during normal operation. However, copper can dissolve if the cell is over-discharged or if local electrode potentials become sufficiently high. Dissolved copper species can migrate through the electrolyte and later deposit elsewhere in the cell. This can increase impedance, disturb the SEI, or in severe cases contribute to internal micro-shorts [12].

Mechanical cracking, corrosion, or loss of contact at the copper current collector also interrupts electronic pathways in the negative electrode. This

causes local current redistribution and can accelerate non-uniform ageing. In Figure 2.1, copper dissolution and copper contact loss are therefore shown as current collector related degradation mechanisms.

The positive electrode is typically coated on an aluminium current collector. Aluminium is generally stable over the normal potential range of the positive electrode, but corrosion can occur under aggressive conditions, such as high potentials, unsuitable electrolyte chemistry, or the presence of corrosive decomposition products. Aluminium corrosion or loss of contact between the positive electrode coating and current collector increases electronic resistance and creates non-uniform current distribution.

### Positive Electrode and Electrolyte Degradation

Ageing is not limited to the negative electrode. At high potentials, the positive electrode can promote electrolyte oxidation and surface-film formation. This cathode-electrolyte interphase can increase impedance and reduce active surface accessibility. The positive electrode can also undergo structural degradation, phase transformation, oxygen release, particle cracking, or transition-metal dissolution, depending on chemistry and operating conditions [12], [13], [20].

Transition-metal dissolution is particularly important for layered oxide positive electrodes. Dissolved Ni, Mn, or Co species can migrate through the electrolyte and reach the negative electrode, where they may deposit or participate in parasitic reactions. This can disturb the SEI and increase impedance.

Electrolyte degradation also contributes to gas formation, impedance rise, surface-film formation, and loss of cyclable lithium. Elevated temperature, high voltage, large polarization, and reactive electrode surfaces can all accelerate electrolyte degradation.

### Internal Short Circuit

The separator is designed to prevent electronic contact between the positive and negative electrodes while allowing ionic transport. If the separator is mechanically damaged, thermally degraded, locally penetrated, or bridged by metallic deposits, an internal short circuit can form. In Figure 2.1, the internal short circuit is illustrated as a dendrite-driven short at the positive electrode side of the separator. However, internal shorts can also be caused

by metallic debris, severe electrode deformation, separator defects, current-collector damage, or manufacturing defects.

An internal short circuit can cause local heat generation, local self-discharge, rapid voltage drop, accelerated degradation, and in severe cases thermal runaway. Even small internal micro-shorts may alter the local current distribution and accelerate heterogeneous ageing.

## Influence of Operating Conditions

The rate and nature of ageing depend strongly on how the battery is used. Important variables include temperature, current rate, voltage limits, SoC window, depth of discharge, rest periods, and mechanical boundary conditions. Low temperature and high charging current increase the risk of lithium plating. High temperature and high voltage promote electrolyte oxidation, SEI growth and gas formation. Wide cycling windows and high depth of discharge increase the amount of active material expansion and contraction, which can accelerate mechanical degradation [14], [19], [20].

In cells with $SiO_x$-containing negative electrodes, the SoC window is particularly important because silicon and graphite do not contribute equally over the full operating range. Some voltage or SoC windows, typically the lower windows, may utilise the silicon-containing fraction more strongly, leading to larger local mechanical stress and faster degradation [14], [15]. Therefore, apparently similar cycling conditions may produce different ageing trajectories depending on the operating window.

## Heterogeneous Ageing

Ageing in a commercial cell is rarely spatially uniform. Differences in local temperature, pressure, electrolyte distribution, current density, or material properties can cause some regions of the cell to degrade faster than others. This is referred to as heterogeneous ageing.

Heterogeneous ageing is particularly important in large-format cylindrical cells. The wound jelly-roll structure, finite tab or current collector geometry, and external cooling boundary conditions make internal gradients difficult to avoid. These gradients can cause local differences in reaction rate, lithium inventory, resistance, mechanical stress, and plating tendency [6], [16], [17].

## 2.3 In-situ Characterisation Techniques

The characterisation methods used in this thesis are mainly non-destructive electrochemical techniques, complemented by structural imaging for selected cells. The purpose is not to identify every ageing mechanism directly, but to track how the cell response changes during ageing and to relate these changes to likely degradation processes.

### Capacity and resistance measurements

The most direct indicators of battery health are capacity and resistance. Capacity measurements quantify the remaining charge that can be delivered by the cell under defined conditions. In ageing studies, capacity is usually measured during reference performance tests using a defined temperature, current rate, and voltage window. The measured capacity depends on the test conditions, so consistent procedures are required when comparing cells and ageing states.

Resistance measurements describe how the voltage responds when current is applied or interrupted. Resistance is important because it determines power capability and heat generation. As the cell ages, resistance generally increases due to SEI growth, surface-film formation, electrolyte transport limitations, loss of contact, and changes in charge-transfer kinetics [18], [19], [23]. Capacity and resistance therefore provide practical SoH indicators, even though they do not uniquely identify the underlying mechanisms.

### Differential Voltage and Incremental Capacity Analysis

Differential voltage analysis (DVA) and incremental capacity analysis (ICA) are derived from slow galvanostatic voltage curves. ICA is defined as

$$\mathrm{ICA} = \frac{\mathrm{d}Q}{\mathrm{d}V}, \tag{2.15}$$

whereas DVA is defined as

$$\mathrm{DVA} = \frac{\mathrm{d}V}{\mathrm{d}Q}. \tag{2.16}$$

In practice, these derivatives are calculated numerically from measured current and voltage data and can be written as

$$\left(\frac{\mathrm{d}Q}{\mathrm{d}V}\right)_i \approx \frac{Q_{i+1} - Q_{i-1}}{V_{i+1} - V_{i-1}}, \tag{2.17}$$

and

$$\left(\frac{\mathrm{d}V}{\mathrm{d}Q}\right)_i \approx \frac{V_{i+1} - V_{i-1}}{Q_{i+1} - Q_{i-1}}. \tag{2.18}$$

These derivative based methods highlight small changes in the voltage response that may be difficult to see in the raw voltage curve. Peaks in ICA correspond to voltage plateaus or phase transitions in the electrode materials, while DVA emphasizes changes in the voltage slope. During ageing, peak shifts, peak broadening, peak intensity changes, and changes in electrode balancing can indicate loss of lithium inventory, loss of active material, or changes in the relative contribution of different active materials [11], [13].

For full cells, the interpretation must be done carefully because the measured voltage is the difference between the positive and negative electrode potentials. A change in a full-cell DVA or ICA feature may therefore originate from either electrode or from a shift in electrode balancing.

## Intermittent Current Interruption

Intermittent current interruption (ICI) is used in this thesis to follow the evolution of cell resistance and diffusion related behaviour during ageing. In ICI, short current interruptions are inserted during constant-current operation. When the current is interrupted, the voltage response contains a rapid voltage change related mainly to ohmic resistance and a slower relaxation related to time-dependent electrochemical and transport processes.

For a current interruption starting at time $t_{\mathrm{int}}$, the elapsed interruption time is defined as

$$\Delta t = t - t_{\mathrm{int}}. \tag{2.19}$$

The voltage change during the interruption may be written as

$$\Delta V(\Delta t) = V(\Delta t) - V_I, \tag{2.20}$$

where $V_I$ is the voltage immediately before the current is interrupted. In the ICI method, the voltage relaxation over a selected time interval is fitted as a function of $\sqrt{\Delta t}$:

$$\Delta V(\Delta t) = -IR_{\mathrm{reg}} - Ik\sqrt{\Delta t}, \tag{2.21}$$

where $I$ is the current before interruption, $R_{\text{reg}}$ is the regression based resistance, and $k$ is a diffusion-related resistance coefficient [18], [23], [24]. If the fitted line is written as

$$\Delta V(\Delta t) = a + b\sqrt{\Delta t}, \tag{2.22}$$

then

$$R_{\text{reg}} = -\frac{a}{I}, \tag{2.23}$$

and

$$k = -\frac{b}{I}. \tag{2.24}$$

A simpler resistance estimate can also be obtained from the voltage change at a fixed time after interruption:

$$R_{\Delta t} = -\frac{\Delta V(\Delta t)}{I}. \tag{2.25}$$

For example, $R_{1\text{s}}$ is obtained from the voltage change after 1 s. However, the regression based resistance $R_{\text{reg}}$ is often more robust because it reduces the dependence on choosing a single arbitrary time point.

The parameter $k$ is related to the slower part of the voltage relaxation and is therefore sensitive to diffusion and other time-dependent processes. In full commercial cells, $k$ should be interpreted as an effective cell-level parameter, because the measured voltage response contains contributions from both the positive and negative electrodes. It is therefore useful for tracking ageing trends, but it should not be interpreted as a direct solid-state diffusion coefficient of one isolated electrode without additional assumptions or electrode-specific measurements.

The ICI method is well suited for repeated measurements during ageing because it provides resistance and diffusion-related information over the voltage or SoC range while remaining simpler and faster than electrochemical impedance spectroscopy or galvanostatic intermittent titration.

## Computed Tomography

X-ray computed tomography scan (CT) provides non-destructive information about the internal structure of a cell. In this thesis, CT is used to examine the jelly roll geometry and structural deformation in selected cylindrical cells. CT can reveal features such as jelly-roll displacement, deformation, voids, cracks,

and core collapse. Such information is difficult or impossible to obtain from voltage and current data alone [17].

CT does not directly identify electrochemical degradation mechanisms such as SEI growth or lithium plating. However, it provides spatial information that can help interpret measurements. For example, a cell showing unusual resistance growth or capacity fade may also show structural changes in the jelly roll. Combining diagnostics with CT can therefore support interpretation of heterogeneous ageing in large cylindrical cells.

# CHAPTER 3

# Experimental Setups and Methodologies

Presented in this chapter are the experimental methodologies and test equipment used in the conducted studies of this thesis.

## 3.1 Test Equipment

**PEC ACT50 Cell tester**
Used for cycling the large-format cells. The tester is designed for a maximum current of 50 A per test channel, a voltage range between 0–5 V, and a maximum logging frequency of 1000 Hz.

**Neware BTS-4000 Cell tester**
Cycling channels on this tester were used to study single-layer cells with different Si–Gr composite electrode materials. The channels have a voltage range between 0–5 V and a maximum current of 6 A. The maximum sampling rate is 10 Hz.

**VALEGRO 350 JULABO Recirculating Cooler**
This recirculating cooler is used for cooling cells. The device can be used for cooling and heating tasks from −20 °C to +40 °C. The pump speed can be adjusted and is specified to offer a constant cooling capacity of 0.35 kW at +20 °C.

## 3.2 Test Objects

**4695 Cylindrical Format Battery Cell**
The 4695 format means that the cell is cylindrical, with a diameter of 46 mm and a height of 95 mm. The electrodes consist of a high-nickel NMC positive electrode together with a Si–Gr composite negative electrode. The cell is rated at 33 Ah capacity and operates between 2.5–4.2 V. The safety vent is located at the bottom of the cell and the cell is therefore designed in a way where bottom cooling is not feasible. The $SiO_x$ content used in manufacturing is unknown.

**PAT-Cell with various electrode configurations**
EL-CELL manufactures electrochemical test equipment such as the PAT-Cell device, which can be used to build two- or three-electrode lithium-ion cells with battery electrode materials. In this thesis, multiple cell variants were built using NMC811 as positive electrode and Artificial Graphite (AG), AG + 5% $SiO_x$, AG + 10% $SiO_x$, and AG + 15% $SiO_x$ as negative electrodes.

## 3.3 Ageing Test Matrix for 4695 Format Cells

The ageing study was designed with various test cases where uniform thermal boundary conditions are compared to cases where thermal gradients are intentionally introduced to study their impact on cell degradation. The resulting test matrix is summarised in Table 3.1. All cycling cases use galvanostatic (CC) charge and discharge rates as listed, with voltage limits between 2.75–4.2 V. This corresponds approximately to a 10–100% SoC range for the lifecycle cycling protocol.

Test cases 1 to 4 provide a baseline set spanning two ambient temperatures, 15 and 25 °C, and two charge C-rates, 0.5C and 0.8C. This set enables

**Table 3.1:** Ageing test matrix for 4695-format cells. Cycling test cases use a 2.75–4.2 V voltage window, corresponding approximately to a 10–100% SoC lifecycle window.

| # | Test case | Chrg | Dchg | Ambient T. | Cooling T. |
|---|---|---|---|---|---|
| 1 | Slow & Cold | 0.5 C | 0.8 C | 15 °C | – |
| 2 | Fast & Cold | 0.8 C | 0.8 C | 15 °C | – |
| 3 | Slow & Warm | 0.5 C | 0.8 C | 25 °C | – |
| 4 | Fast & Warm | 0.8 C | 0.8 C | 25 °C | – |
| 5 | Cooling lower third | 0.8 C | 0.8 C | 15 °C | 5 °C |
| 6 | Cooling upper third | 0.8 C | 0.8 C | 15 °C | 5 °C |

separation of temperature-driven effects from rate-driven effects under approximately uniform thermal conditions, and it establishes reference ageing trajectories for comparison against heterogeneous cases.

Test cases 5 to 6 introduce deliberate non-uniform cooling on the side of the cell to generate repeatable temperature gradients along the lateral surface. Both cases are operated in a 15 °C chamber while applying local cooling at 5 °C to either the lower or upper half of the can surface. By keeping the electrical protocol fixed, these tests isolate the influence of temperature gradients on ageing signatures and enable assessment of whether degradation becomes localised depending on the direction and location of cooling.

## 3.4 Test Protocol

To track performance evolution during ageing, a Reference Performance Test (RPT) was performed every 20 days. The RPT consists of a C/20 capacity measurement followed by an ICI sequence at C/10. The lifecycle cycling protocol and the RPT procedure are summarised in Tables 3.2 and 3.3.

The lifecycle cycling protocol was performed between 2.75–4.2 V, corresponding approximately to a 10–100% SoC cycling range. The RPT was performed at 25 °C to provide comparable diagnostic measurements independent of the ageing temperature.

**Table 3.2:** Lifecycle cycling protocol with a voltage window between 2.75–4.2 V.

| Step | Mode | Rate | Limit / time |
|---|---|---|---|
| 1 | Discharge (CC) | 0.8C | 2.75 V |
| 2 | Rest | – | 15 min |
| 3 | Charge (CC) | 0.5C or 0.8C | 4.2 V |
| 4 | Rest | – | 15 min |

**Table 3.3:** Reference Performance Test protocol performed every 20 days at 25 °C.

| Block | Mode | Rate | Limit / time |
|---|---|---|---|
| Pre-RPT | Discharge (CC) | 0.5C | 2.5 V |
| Pre-RPT | Rest | – | 15 min |
| Pre-RPT | Discharge (CC) | C/20 | 2.5 V |
| Pre-RPT | Rest | – | 30 min |
| C/20 capacity | Charge (CC) | C/20 | 4.2 V |
| C/20 capacity | Rest | – | 30 min |
| C/20 capacity | Discharge (CC) | C/20 | 2.5 V |
| C/20 capacity | Rest | – | 30 min |
| ICI (C/10) | Charge (CC) | 0.1C | 4.2 V |
| ICI (C/10) | Charge (CV) | C/20 cutoff | 4.2 V |
| ICI (C/10) | Rest | – | 30 min |
| ICI (C/10) | Discharge (CC) | 0.1C | 2.5 V |
| ICI (C/10) | Rest | – | 30 min |

## 3.5 Cooling System for Temperature Gradients

Temperature gradients lead to variations in the local current density and heat generation, potentially accelerating degradation in specific regions even when the overall cell temperature remains within nominal limits. To investigate

these effects in a controlled manner, a dedicated cooling system was developed to induce repeatable temperature gradients on 4695-format cylindrical cells.

The concept is to combine a temperature-controlled chamber environment with a local cooling interface that contacts only a defined portion of the cell can. By restricting the cooled area to either the lower or upper part of the can surface, the setup enables comparison between different gradient directions while keeping the cycling protocol and ambient temperature constant. The coolant temperature is controlled independently with a recirculating water cooler.

Figure 3.1 shows the chamber-level arrangement, while Figures 3.2a and 3.2b illustrate the local cooling interface and its placement on the 4695 cell, covering one third of its height. Together, the setup forms the experimental basis for the heterogeneous test cases in Table 3.1, enabling repeatable boundary conditions for studying the influence of temperature gradients on degradation behaviour.

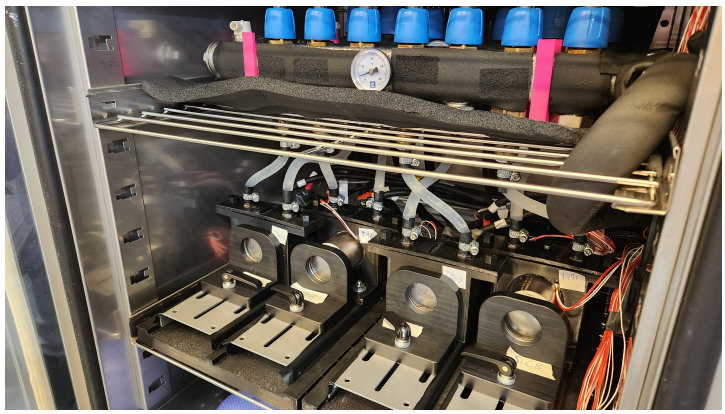

**Figure 3.1:** Environmental chamber setup used to control the ambient air temperature during cycling while applying localised cooling to the cell surface.

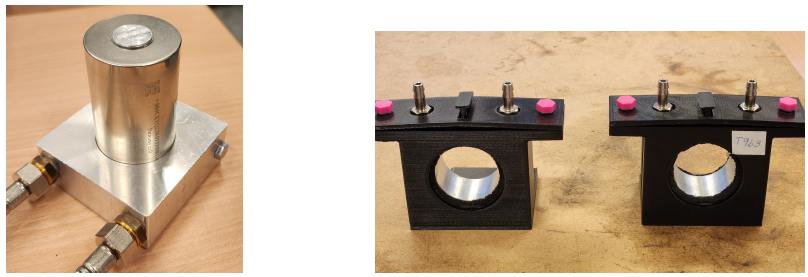

**(a)** Cooling interface mounted on the cell.

**(b)** Cooling block geometry with insulating parts.

**Figure 3.2:** Localised cooling setup used to impose temperature gradients on the 4695-format cell.

## 3.6 Silicon-Graphite Composite Cells

To complement the large-format 4695 cell experiments, laboratory scale Si–Gr composite cells were studied to isolate material-level effects associated with introducing silicon oxide into the negative electrode. The electrochemical cells were assembled using PAT-Cell hardware manufactured by EL-CELL, as shown in Figure 3.3. The purpose of these tests was to establish reference voltage signatures for graphite and $SiO_x$-containing composite electrodes under controlled laboratory conditions. These reference measurements are later used to support interpretation of the 4695-format cell response.

The laboratory cells were assembled as three-electrode cells using an NMC811 positive electrode and different negative electrode compositions: artificial graphite (AG), AG + 5% $SiO_x$, AG + 10% $SiO_x$, and AG + 15% $SiO_x$ with similar areal capacity. The three-electrode configuration included an insulation sleeve with a lithium reference ring and a 0.26 mm glass fiber Whatman separator. The electrolyte was a 1.2 M $LiPF_6$ solution in a carbonate based solvent mixture. The solvent composition was ethylene carbonate (EC), ethyl methyl carbonate (EMC), and fluoroethylene carbonate (FEC) in a 27:63:10 weight ratio, with 2 wt.% vinylene carbonate (VC) added as an electrolyte additive.

All Si–Gr laboratory cell tests were conducted at 25 °C. The full voltage range of 2.5–4.2 V was defined as the 0–100% SoC window for the full-cell cycling.

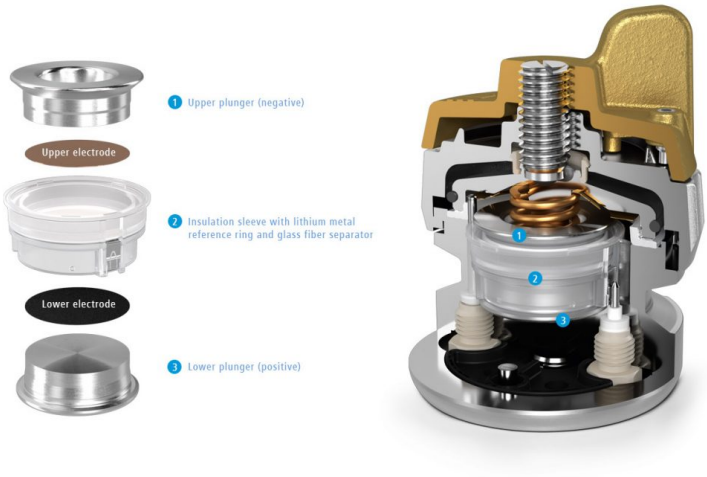


**Figure 3.3:** PAT-Cell structure designed and manufactured by EL-CELL. This illustration is borrowed from EL-CELL's homepage [25].

The main electrode properties used in the cell study are summarised in Table 3.4. The negative electrodes differ in $SiO_x$ content, specific capacity, and coating weight, while the positive electrode used in the present study was NMC811.

**Table 3.4:** Electrode properties used for the laboratory-scale Si–Gr composite cells.

| **Electrode** | **Material** | **Capacity** ($\mathbf{mAh\,g^{-1}}$) | **Coating weight** ($\mathbf{mg\,cm^{-2}}$) |
|---|---|---|---|
| Positive electrode | NMC811 | 183.0 | 20.0 |
| Negative electrode | AG | 340 | 12.89 |
| Negative electrode | AG + 5% $SiO_x$ | 393 | 11.22 |
| Negative electrode | AG + 10% $SiO_x$ | 445 | 9.95 |
| Negative electrode | AG + 15% $SiO_x$ | 498 | 8.91 |

The cell configurations selected for lifecycle testing are shown in Table 3.5.

The 15% $SiO_x$ cells were cycled over three different SoC windows to investigate how the utilised voltage region affects the response of the Si–Gr composite electrode. In addition, graphite-only cells were cycled over the full 0–100% SoC window to provide a baseline without silicon oxide.

**Table 3.5:** Lifecycle test matrix for the laboratory Si–Gr composite cells with 0.5 C charge and 0.5 C discharge rate.

| **Negative electrode** | **SoC window** | **Replicates** |
|---|---|---|
| AG + 15% $SiO_x$ | 0–50% | 2 |
| AG + 15% $SiO_x$ | 50–100% | 2 |
| AG + 15% $SiO_x$ | 0–100% | 2 |
| AG | 0–100% | 2 |

Before lifecycle cycling, each cell was subjected to three formation cycles between 2.5–4.2 V using constant-current charge and discharge. The formation current was C/10, corresponding to 0.888 mA for these laboratory cells. The formation protocol is summarised in Table 3.6.

**Table 3.6:** Formation protocol for the laboratory Si–Gr composite cells.

| **Step** | **Mode** | **Current** | **Limit** |
|---|---|---|---|
| 1 | Charge (CC) | C/10, 0.888 mA | 4.2 V |
| 2 | Discharge (CC) | C/10, 0.888 mA | 2.5 V |

The lifecycle protocol consisted of repeated 0.5C charge and discharge cycling within the assigned SoC window. A Reference Performance Test (RPT) was performed every 40 cycles. The RPT included a low-rate C/20 capacity sequence and an ICI sequence at C/10. The RPT protocol is summarised in Table 3.7.

**Table 3.7:** Reference Performance Test protocol for the laboratory Si–Gr composite cells, performed every 40 lifecycle cycles.

| **Block** | **Procedure** | **Rate** |
|---|---|---|
| Capacity test | Discharge–charge–discharge | C/20 |
| ICI test | Charge–discharge with current interruptions | C/10 |

The resulting datasets serve two purposes. First, they identify how $SiO_x$ content and cycling window affect characteristic voltage signatures in controlled laboratory cells. Second, they provide reference behaviour for interpreting the 4695-format cell, where the exact $SiO_x$ content of the negative electrode is unknown.

# CHAPTER 4

# Electrochemical Signatures of Cells Containing $SiO_x$

Blended negative electrodes containing $SiO_x$ differ from negative electrodes containing only graphite in both their capacity contribution and their full cell voltage response. This chapter first establishes BoL electrochemical reference signatures using laboratory cells containing nominal $SiO_x$ fractions of 0%, 5%, 10%, and 15%. These reference signatures are then compared with those of a prototype 4695 cell for which the exact negative electrode composition was not independently measured. The purpose of this comparison is to identify which laboratory reference composition that provides the closest electrochemical response. The second part of the chapter examines the ageing of 15% Si–Gr cells cycled over different nominal SoC windows, together with graphite-only reference cells.

## 4.1 Beginning of Life Electrochemical Signatures

### Voltage Curves and Hysteresis as a Function of $SiO_x$ Content

At beginning of life, the clearest differences between the studied laboratory cells are observed in the charge and discharge voltage curves obtained during

slow cycling. As the nominal $SiO_x$ fraction increases, the shape of the full cell voltage profile changes, particularly in the region where the silicon-containing phase contributes to lithium storage in the negative electrode.

Figure 4.1 is plot of full cell voltage as a function of SoC for laboratory cells containing nominal $SiO_x$ fractions of 0, 5, 10, and 15%. The cells were charged and discharged at C/20. The differences between the voltage profiles are most apparent in the low SoC region, where the separation between the charge and discharge curves increases with $SiO_x$ content. The resulting hysteresis profile can therefore be treated as a practical fingerprint when cells are compared using the same cycling protocol.

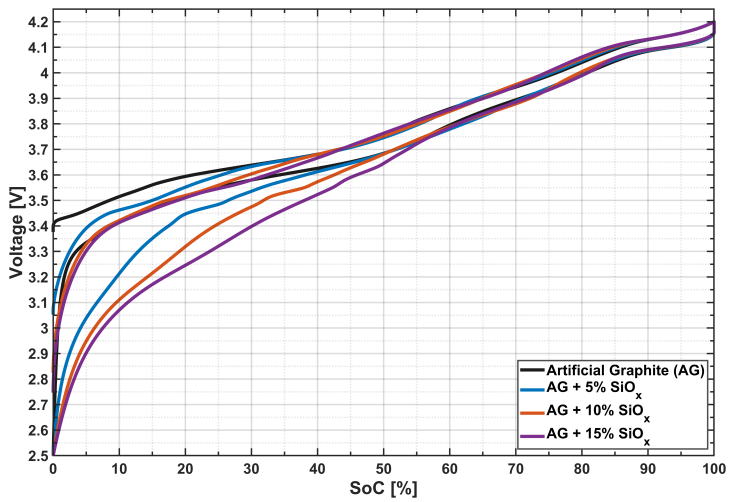


**Figure 4.1:** Charge and discharge voltage profiles of four cells with different $SiO_x$ content. AG, AG + 5%$SiO_x$, AG + 10% $SiO_x$, AG + 15% $SiO_x$.

Figure 4.2 shows the full cell voltage hysteresis as a function of SoC. The hysteresis was calculated as the difference between the charge and discharge voltages at the same SoC. The laboratory reference cells are compared with the prototype 4695-format cell studied in this thesis.

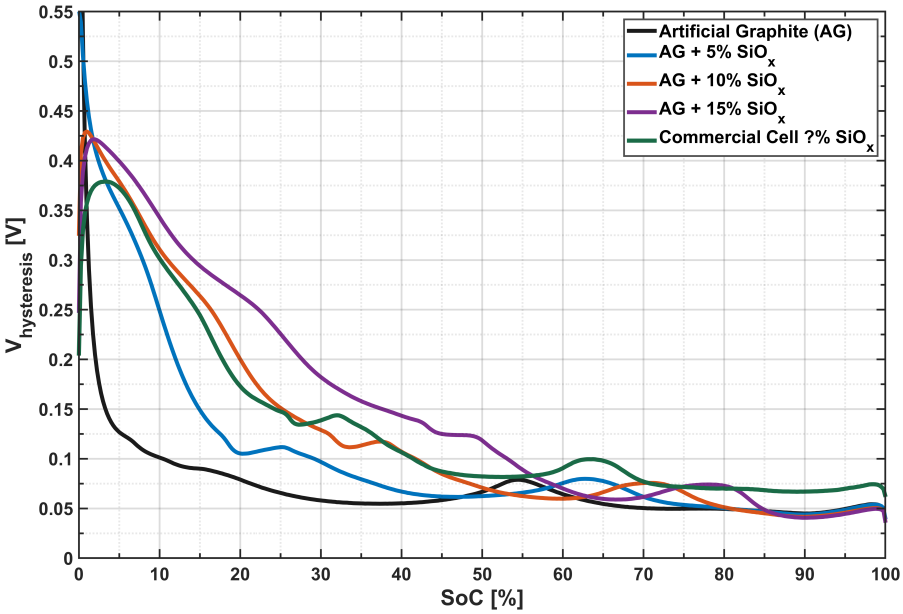


**Figure 4.2:** Voltage hysteresis obtained from C/20 charge–discharge cycles for laboratory cells containing nominal $SiO_x$ fractions of 0, 5, 10, and 15%, compared with the prototype 4695 cell.

The results show the expected overall trend that the full cell voltage hysteresis increases as the $SiO_x$ content increases. Unlike graphite, which stores lithium mainly through intercalation between graphitic layers, silicon-containing materials store lithium through alloying reactions that involve larger structural and volume changes. Lithiation and delithiation therefore follow different electrochemical and mechanical pathways, producing a larger difference between the charge and discharge potentials. Increasing the $SiO_x$ fraction increases the proportion of the negative electrode capacity associated with this reaction. Consequently, the graphite-only cell shows the lowest hysteresis, the 15% $SiO_x$ cell shows the highest, and the 5 and 10% $SiO_x$ cells lie between them.

The separation between the cells is most pronounced in the low SoC regions. In this part of the full cell response, the silicon-containing phase makes a comparatively strong contribution to the negative electrode voltage, making

its larger lithiation–delithiation hysteresis clearly visible. At higher SoC, the relative influence of graphite and the positive electrode response becomes more pronounced, and the hysteresis curves therefore move closer together.

The ordering of the curves is not perfectly monotonic at every SoC, and several local peaks and changes in slope are observed. This is expected because the measured hysteresis is made on a full cell which contains contributions from both electrodes. It is affected by electrode balancing and polarisation. Nevertheless, the overall separation between the reference cells is sufficiently clear for their hysteresis profiles to be used as qualitative electrochemical fingerprints.

Among the investigated laboratory references, the 4695-format cell hysteresis shows the closest visual agreement with the nominal 10% $SiO_x$ cell over much of the low and intermediate SoC range. However, the 4695-format cell exhibits some differences that is not reproduced identically by the laboratory cell. Such deviations are expected because the 4695-format cell uses a higher nickel-based positive electrode NMC9xx, whereas the laboratory cells use NMC811. The cells also differ in electrode balancing, electrolyte composition, and mechanical cell attributes.

The comparison can therefore be interpreted as an electrochemical similarity assessment rather than as an independent quantitative measurement of the $SiO_x$ content. Among the four available reference compositions, the 4695-format cell behaves most similarly to the 10% $SiO_x$ reference. This observation is consistent with supplier provided information indicating a $SiO_x$ content of approximately 10%.

The transferability of the laboratory cell results to the 4695-format cell has some limitations. The laboratory reference series contains only four discrete compositions, and the full-cell hysteresis cannot uniquely separate the influence of the negative electrode composition from differences in the remaining cell design. Independent material characterisation would be required to determine the 4695-format cell $SiO_x$ fraction quantitatively. Nevertheless, the clear separation between the graphite-only and $SiO_x$-containing laboratory cells demonstrates that slow cycle voltage hysteresis provides a useful qualitative fingerprint of a silicon-containing negative electrode.

## 4.2 Ageing in Different State of Charge Windows

After establishing the BoL fingerprints, the next question is how the Si–Gr cells age in various SoC windows.

The investigated nominal cycling windows were 0–50% SoC, referred to as the low SoC window; 50–100% SoC, referred to as the high SoC window; and 0–100% SoC, referred to as the full SoC window. The Si–Gr cells contained a nominal $SiO_x$ fraction of 15%. Graphite-only cells cycled over the full SoC range were included as a reference.

Figure 4.3 is a line plot of capacity-based SoH as a function of full equivalent cycles. Two individual cell trajectories are shown for each test condition. Plotting the results against full equivalent cycles normalises the comparison with respect to charge throughput and allows cells cycled over different depth of discharge windows to be compared on a common basis.

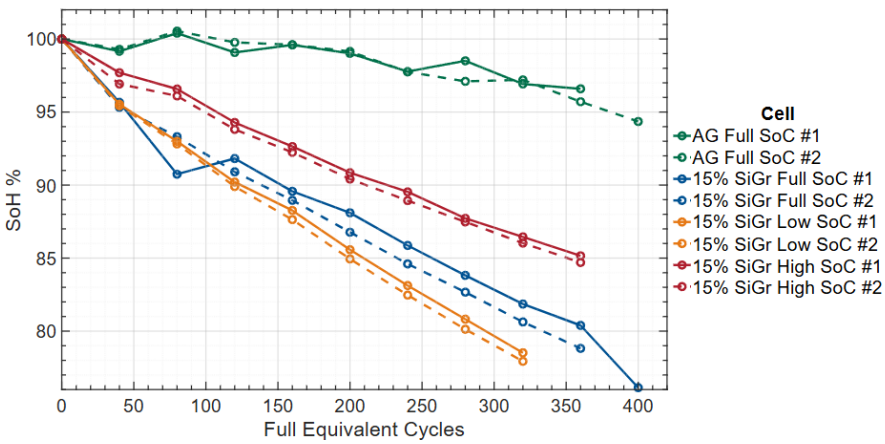


**Figure 4.3:** SoH as a function of full equivalent cycles for graphite-only cells cycled over the full SoC range and 15% Si–Gr cells cycled over 0–50%, 50–100%, and 0–100% SoC windows. Two cells are cycled for each condition.

The graphite-only reference cells show substantially better capacity retention than all three $SiO_x$–graphite conditions. After approximately 400 full equivalent cycles, the graphite cells retain approximately 94–96% of their BoL capacity. In comparison, the Si–Gr cells show a considerably faster reduction

in SoH. This separation indicates that the presence and utilisation of the silicon-containing phase strongly affect the ageing response under the investigated conditions.

Among the Si–Gr cells, cycling in the nominal low SoC window generally produces the fastest capacity loss. The low SoC cells reach 80% SoH after roughly 290 full equivalent cycles. The full SoC window cells show a similar but generally slightly slower degradation trend reaching 80% SoH near 350 full equivalent cycles. The cells cycled in the high SoC window show the best capacity retention among the cases, retaining 85% SoH after around 360 full equivalent cycles. The test ended before reaching 80% SoH since there was no more time to continue cycling.

The stronger degradation in the low SoC window is consistent with the BoL hysteresis results in Figure 4.2. The largest differences between graphite and the $SiO_x$-containing cells occur in the lower part of the SoC range. This indicates that the relative contribution of the silicon-containing phase, or the electrochemical processes associated with it, is particularly pronounced in this region. Repeated cycling through this SoC region can expose the $SiO_x$ domains to repeated volume changes. These changes can promote particle or electrode level mechanical damage, rupture and reformation of the SEI, loss of cyclable lithium, and gradual loss of active material.

Full window cycling also produces substantial degradation because it repeatedly uses a broad range of the negative electrode capacity and includes the region where the $SiO_x$ contribution is pronounced. The high SoC window appears to avoid part of the most damaging low SoC response and therefore shows slower capacity loss.

Although full equivalent cycles account for differences in charge throughput, they do not make the physical number of cycles identical. A cell cycled over a 50%-wide SoC window undergoes approximately twice as many charge–discharge cycles as a full window cell for the same number of full equivalent cycles. Repeated mechanical loading may therefore contribute to the faster degradation of the partial window cells. However, both the low and high SoC conditions use a 50% wide window, while their ageing rates differ substantially.

The two cells within each test condition show broadly similar degradation trends, although some cell-to-cell variation is visible. Since two replicates were available for each condition, the result can be interpreted as evidence of repeatability.

Transfer of the ageing-window result to the 4695-format cell should be made cautiously. The laboratory and 4695-format cells differ in cell geometry, electrode loading, electrode balancing, pressure, electrolyte composition, positive electrode chemistry, and thermal conditions. Furthermore, the 4695-format cell contains approximately 10% $SiO_x$, whereas the ageing-window study used laboratory cells containing nominally 15% $SiO_x$. The laboratory results are therefore only used as a controlled reference showing how Si–Gr ageing signatures look like and can depend strongly on the utilised SoC window.

## Evolution of Electrochemical Signatures During Ageing

To complement the capacity-based SoH results, the evolution of the ICA curves are examined for the graphite-only reference cells and for the 15% Si–Gr cells cycled in the low, high, and full SoC windows. The ICA profiles obtained from C/20 charge and discharge cycles are shown at beginning of life and at selected ageing states in Figure 4.4.

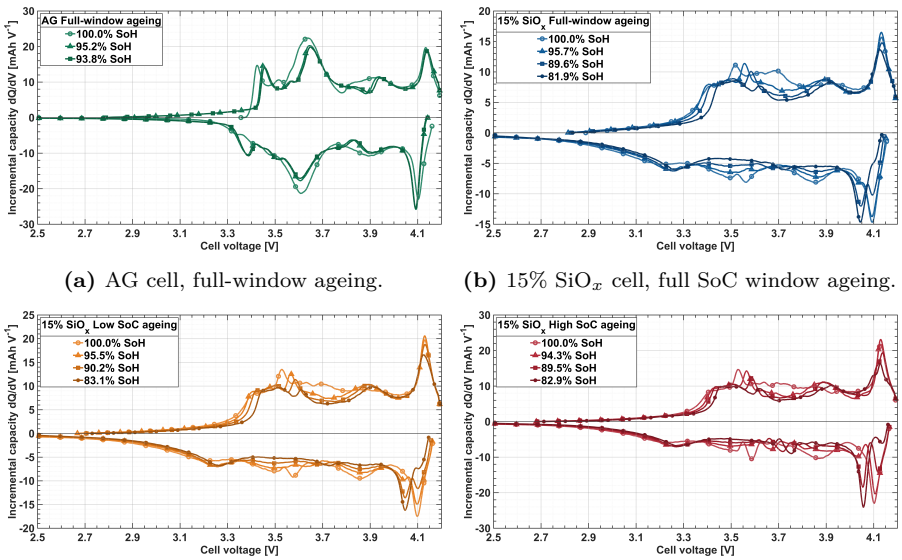


**(a)** AG cell, full-window ageing.

**(b)** 15% $SiO_x$ cell, full SoC window ageing.

**(c)** 15% $SiO_x$ cell, low SoC window ageing.

**(d)** 15% $SiO_x$ cell, high SoC window ageing.

**Figure 4.4:** Incremental capacity analysis obtained from C/20 cycling. The profiles are shown at beginning of life and at selected ageing states.

The graphite-only reference shows comparatively limited evolution of the ICA profile during the investigated ageing period. The main features remain at similar voltages and retain much of their initial sharpness. This is consistent with the capacity results in Figure 4.3, where the graphite-only cells retained a substantially higher SoH than the Si–Gr cells.

For all three 15% Si–Gr cells, decreasing SoH is accompanied by changes in the position and shape of the ICA features. These changes show that the capacity contribution of the underlying full cell reactions is changed across the voltage range as cell ages.

A decrease in peak height should not, by itself, be interpreted as direct loss of active material. In ICA, the capacity associated with a reaction region is more closely related to the integrated area of the feature than to its maximum value. Peak broadening can therefore reduce the peak height without an equivalent loss of capacity. Similarly, a voltage shift may result from changes in electrode balancing, loss of lithium inventory, increased polarization, or a combination of these effects.

The ICA profiles of the low-, high-, and full SoC window aged Si–Gr cells show broadly similar changes when compared at approximately the same SoH. Local differences in peak position and amplitude are visible, but they are not sufficiently systematic to identify separate degradation mechanisms for the three cycling windows. In particular, the present ICA results do not provide clear evidence that one SoC window causes a unique form of electrochemical degradation.

The clearer distinction between the test cases is therefore the rate at which capacity is lost. The SoH results show that the cells reach comparable ageing states at different rates, whereas the ICA results indicate that their full cell electrochemical signatures evolve in a broadly similar direction. The SoC window may therefore primarily affect the rate at which the observed degradation develops, rather than producing a clearly different ICA fingerprint at a given SoH.

# CHAPTER 5

# Ageing of Cylindrical 4695-format Cells

This chapter turns to the prototyped 4695-format cells and documents their ageing history. The aim is to describe the main trends in capacity fade, resistance growth, thermal response, and selected electrochemical signatures. Several tests were still ongoing or were stopped before the cells reached 80% SoH. The results are therefore interpreted as an interim and descriptive comparison of the available data.

## 5.1 Test Matrix Overview

The cells were aged using galvanostatic protocols that varied ambient temperature, current rate, and cooling configuration. The reference protocol used the 0.5C/0.8C condition, while the higher rate protocol used 0.8C/0.8C. Reference and higher rate tests were performed at 15 °C and 25 °C. Additional cells were tested at 15 °C using partial side cooling on lower and upper cell configurations. Two cells were assigned to each condition. The exact conditions and RPT are defined in Chapter 3.3 and 3.4.

## 5.2 Cell Capacity

Before ageing, the cells showed a spread in measured capacity. Figure 5.1 shows the BoL capacity deviation. The SoH curves presented later are normalised to the individual BoL capacity of each cell. This enables direct comparison of relative capacity fade, but it removes information about differences in absolute starting capacity. A cell with a lower initial capacity can therefore begin at 100% SoH in the same way as a cell with a higher initial capacity.

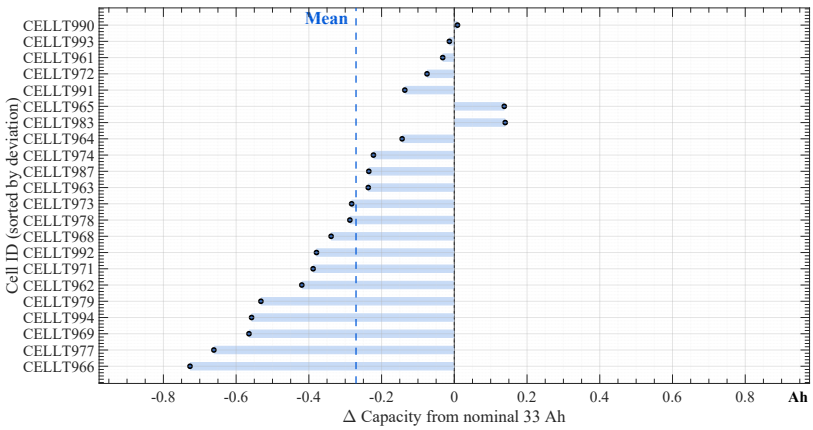


**Figure 5.1:** BoL capacity deviation from rated capacity of the prototype 4695-format cells.

### Capacity Retention Under Galvanostatic Ageing

Figure 5.2 shows capacity retention relative to BoL as a function of EFC. All cells begin at 100% by definition, and the trajectories remain comparatively close during early life. The separation becomes progressively larger after approximately 200 EFC. By the end of the observed tests, the lifetime spread is substantial. The earliest cell approaches the 80% criterion after approximately 350 EFC, whereas the longest lived completed trajectories approach the same criterion after approximately 1000 EFC.

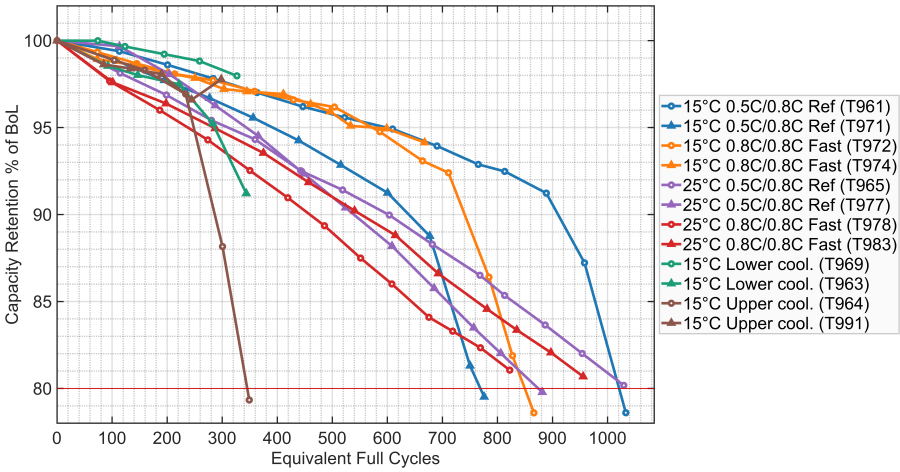


**Figure 5.2:** Capacity retention of the 4695 cells as a function of equivalent full cycles. Capacity is normalised to the individual BoL value. The horizontal line denotes the nominal 80% EoL criterion.

Two broad trajectory types are visible. Several cells show a comparatively smooth and approximately linear decline over most of the measured range. This behaviour is most evident for the 25 °C cells. Other cells cycled at lower temperatures show an apparent transition from slow fade to accelerated fade referred to as an apparent knee. Clear examples are T961, T971, T972, T963 and T964.

The early life ranking does not reliably predict the late life ranking. T964, for example, remains within the main population during early life but later undergoes rapid capacity loss. Conversely, T961 and T972 develops a late knee but remains one of the longest lived cells in the dataset. A low initial fade rate is therefore not sufficient evidence of a long lifetime.

### Comparison of the 15 °C Reference Cells

The two 15 °C reference cells, T961 and T971, show one of the largest variations cycled under same conditions. T971 begins to depart from the slower trajectory early in its lifetime and shows pronounced acceleration near 680–700 EFC. It reaches the 80% region at approximately 770 EFC. T961 retains more than 90% capacity until close to 900 EFC and then exhibits a steep

decline, crossing the 80% level at approximately 1020 EFC. The difference between the two nominal replicates is therefore approximately 250 EFC. To explore the cause for this ageing behavior, a thorough cell teardown analysis must be performed. This pair demonstrates that the same nominal condition can produce substantially different late life behaviour.

### Comparison of the 15 °C Higher Rate Cells

T972 follows a relatively gradual fade until approximately 700 EFC, after which the trajectory steepens sharply. The cell crosses the 80% level at approximately 850 EFC. T974 remains among the higher retention cells over the available interval and is still at approximately 94% after about 670 EFC. Since T974 does not reach end of life in this dataset, the pair cannot yet be used to calculate a complete condition level lifetime distribution.

The available data do not show a simple and systematic penalty from increasing the first rate from 0.5C to 0.8C at 15 °C. T972 lies between the two completed reference cell lifetimes, while T974 has not yet shown an equivalent late life decline.

### Comparison of the 25 °C Reference and Higher Rate Cells

At 25 °C, the two reference cells show gradual but distinct trajectories. T965 approaches the 80% criterion at approximately 1030 EFC, while T977 reaches the same region at approximately 880 EFC. The difference between the cells is therefore approximately 150 EFC. In contrast to the abrupt terminal changes observed for several 15 °C cells, the decline of the 25 °C reference cells is comparatively smooth and linear.

The 25 °C higher rate cells have a similar lifetime trajectory. T978 ends slightly above 80% at approximately 820 EFC, while T983 remains slightly above 80% at approximately 960 EFC. The spread within the reference pair and within the higher rate pair is comparable to the separation between the two conditions.

### Comparison Between 15 °C and 25 °C

The best completed 15 °C and 25 °C trajectories, T961 and T965, both approach the 80% criterion near 1000 EFC. Likewise, shorter lived cells are present at both temperatures.

The stronger temperature related observation concerns the shape and variability of the trajectories rather than only their endpoint. The 25 °C cells generally show smoother capacity loss, whereas several 15 °C cells show more abrupt late life acceleration and larger divergence between nominal replicates.

### Effect of the Cooling Configuration

The modified 5 °C to 15 °C cooling cases show the most extreme behaviour in the dataset. T964, tested with the upper cooling configuration, follows the main population until approximately 230–260 EFC and then undergoes a rapid decline, reaching the 80% region near 350 EFC. T963, tested with the lower cooling configuration, also accelerates after approximately 270 EFC and falls to about 91% by approximately 345 EFC. These trajectories indicate that the thermal boundary condition can be associated with substantially earlier degradation than observed for the reference cases.

The paired cells do not, however, show uniform behaviour. T969 remains near 98% over the approximately 330 EFC shown, and the available T991 data are incomplete. The present results therefore do not justify a general statement that either lower or upper cooling is intrinsically superior.

Table 5.1 summarises the principal observations from Figure 5.2.

**Table 5.1:** Descriptive summary of the capacity retention trajectories. Approximate values are attained from Figure 5.2.

| Condition | Cell | Final Point | Characteristic |
|---|---|---|---|
| 15 °C, 0.5C/0.8C | T961 | 1020 EFC at 80% SoH | Late sharp knee. |
| | T971 | 770 EFC at 80% SoH | Earlier sharp knee. |
| 15 °C, 0.8C/0.8C | T972 | 850 EFC at 80% SoH | Clear knee. |
| | T974 | 670 EFC at 94% SoH | Smooth but incomplete. |
| 25 °C, 0.5C/0.8C | T965 | 1030 EFC at 80% SoH | Near linear fade. |
| | T977 | 880 EFC at 80% SoH | Near linear fade. |
| 25 °C, 0.8C/0.8C | T978 | 820 EFC at 81% SoH | Near linear fade. |
| | T983 | 960 EFC at 81% SoH | Near linear fade. |
| 15 °C, with 5 °C lower cooling | T969 | 330 EFC at 98% SoH | Low fade but incomplete. |
| | T963 | 345 EFC at 91% SoH | Early strong knee. |
| 15 °C, with 5 °C upper cooling | T964 | 350 EFC at 80% SoH | Earliest EoL. |
| | T991 | – | Incomplete dataset. |

## 5.3 Evolution of the Galvanostatic Cycling SoC Window

The SoH results describe the low rate capacity retained during the RPTs, but they do not directly show how much of that capacity remains accessible during the voltage limited galvanostatic ageing cycles. The lower and upper SoC boundaries were therefore reconstructed for each available ageing point. The cycling window width is defined as

$$\Delta \mathrm{SoC}_{\mathrm{CC}} = \mathrm{SoC}_{\mathrm{upper}} - \mathrm{SoC}_{\mathrm{lower}}. \tag{5.1}$$

At fixed voltage limits, an increase in cell or contact resistance increases the voltage drop. During charge, the upper voltage limit is then reached at a lower true SoC. During discharge, the lower voltage limit is reached at a higher true SoC. A growing polarisation contribution is therefore expected to contract the accessible cycling window.

#### 15 °C Reference and Higher Rate Conditions

For the reference cells shown in Figure 5.3a, the lower SoC boundary remains comparatively stable, generally between approximately 8% and 13% SoC. The reduction in the cycling window is therefore mainly caused by the upper boundary shifting to lower SoC.

For T961, the upper boundary decreases gradually from approximately 76% SoC at BoL to approximately 69% SoC at the final measurement. The lower boundary changes only slightly, and the total cycling window therefore contracts by approximately 8 percentage points. The window contraction develops gradually and is visible before the pronounced SoH decline that begins near 900 EFC in Figure 5.2.

T971 shows a similar total reduction in window width, but the change occurs earlier. The upper boundary decreases from approximately 74% SoC at BoL to approximately 65% SoC at the final measurement. The strongest decrease occurs during the later part of the test, from approximately 70% SoC at 600 EFC to approximately 65% SoC near 760 EFC. This corresponds to the period in which the SoH trajectory of T971 begins to accelerate.

The earlier contraction of the cycling window is therefore consistent with the earlier SoH knee of T971. However, T961 and T971 show a similar total

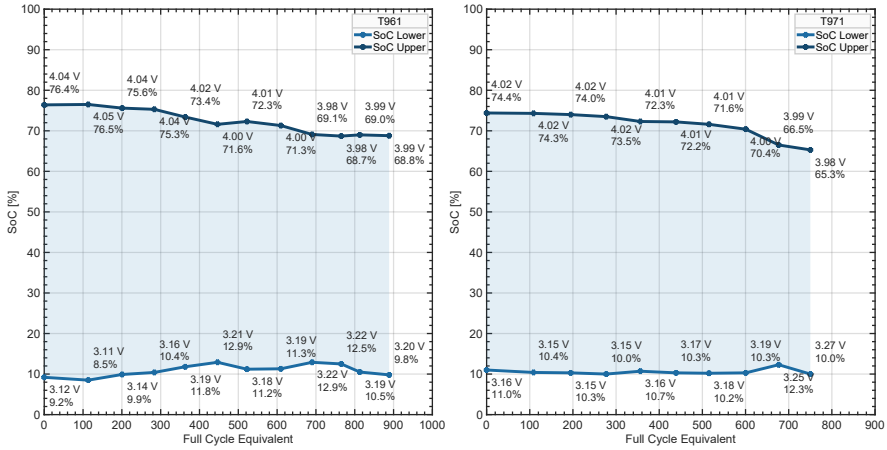


**(a)** 0.5C/0.8C reference cells T961 and T971.

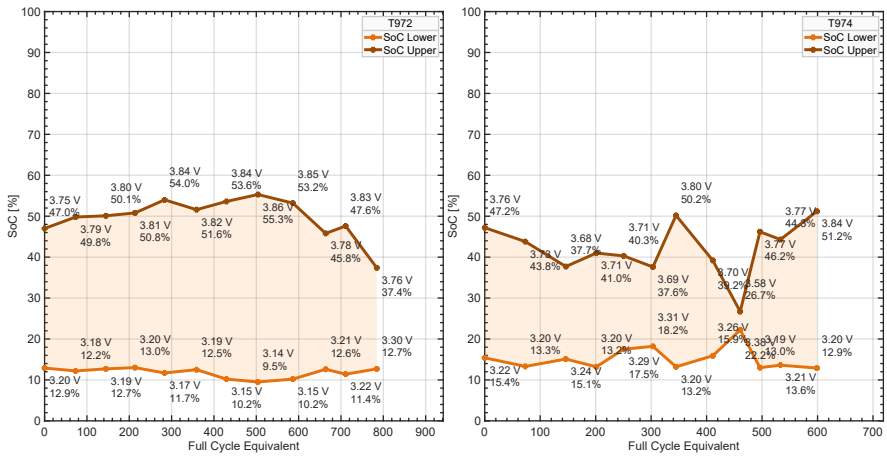


**(b)** 0.8C/0.8C higher rate cells T972 and T974.

**Figure 5.3:** Evolution of the galvanostatic cycling SoC window for cells aged at 15 °C under the reference and higher-rate conditions.

window contraction despite their different lifetimes. T961 reaches 80% SoH approximately 250 EFC later than T971. The window width alone therefore does not fully explain the difference between the two cells.

The higher-rate cells in Figure 5.3b show more distinct behaviour. For T972, the cycling window initially becomes wider because the upper boundary increases from approximately 47% to 55% SoC during the first part of the test. After approximately 600 EFC, the upper boundary decreases rapidly. At the final measurement, it has fallen to approximately 37% SoC, while the lower boundary remains close to 13% SoC. Consequently, the cycling window decreases from a maximum width of approximately 46 percentage points to approximately 25 percentage points.

This rapid late life contraction occurs during the same general period as the pronounced SoH knee of T972, which becomes visible after approximately 700 EFC in Figure 5.2. The agreement between the two trends suggests that the accelerated capacity loss is accompanied by a substantial reduction in the SoC range accessible during galvanostatic cycling.

T974 behaves differently from the other cells. Both the upper and lower SoC boundaries vary strongly and non-monotonically. At one measurement, the window temporarily decreases to only a few percentage points, after which it reopens substantially. Such a response is not consistent with a simple, gradual ageing process.

One possible explanation is a combination of poor cell quality and high or variable electrical contact resistance. Additional contact resistance increases the measured terminal voltage drop and can cause the upper and lower voltage limits to be reached earlier. If the contact resistance changes between measurements, the reconstructed SoC window may appear to contract and later reopen.

#### 25 °C **Reference and Higher Rate Conditions**

The 25 °C cells generally show smoother window evolution, consistent with the smoother SoH trajectories in Figure 5.2. For T965 in Figure 5.4a, the upper boundary decreases from approximately 76% to 66% SoC, while the lower boundary remains close to 9%–10%. The resulting window contracts gradually by approximately 11 percentage points. This continuous change is consistent with its near linear SoH decline.

T977 initially follows the same general trend. Its upper boundary decreases

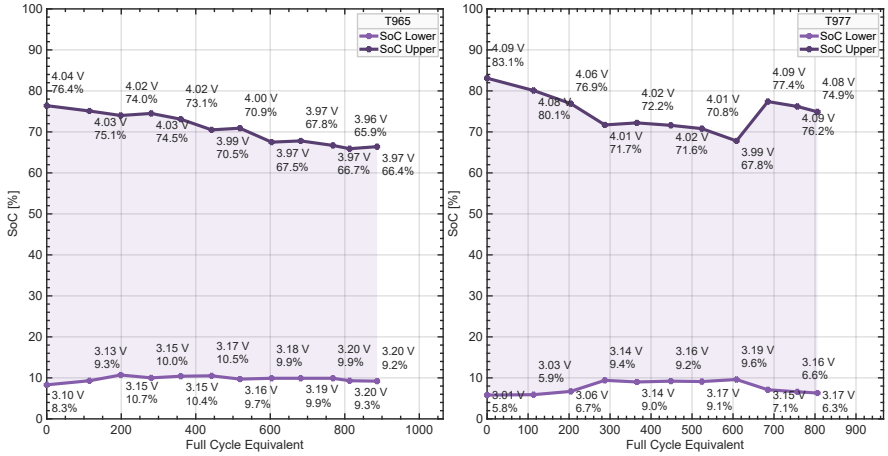


**(a)** 0.5C/0.8C reference cells T965 and T977.

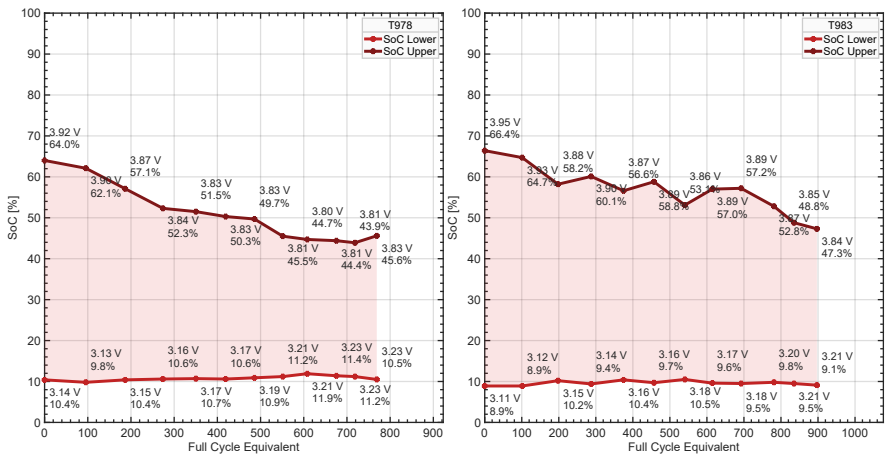


**(b)** 0.8C/0.8C higher rate cells T978 and T983.

**Figure 5.4:** Evolution of the galvanostatic cycling SoC window for cells aged at 25 °C under the reference and higher-rate conditions.

from approximately 83% to 68% SoC by approximately 600 EFC. The window then partially reopens near 680 EFC. This reopening is not mirrored by a corresponding recovery in the SoH trajectory. It may therefore reflect a reversible change in polarisation, a test interruption or changed contact resistance conditions.

For the higher rate cells in Figure 5.4b, the window contracts progressively and is again dominated by the upper boundary. T978 decreases from a window of approximately 54 percentage points to approximately 33 percentage points. T983 decreases from approximately 58 to 38 percentage points, with modest intermediate fluctuations. These gradual contractions are consistent with the capacity fade of both cells. Compared with T965, the higher rate cells show a larger loss of accessible cycling window, even though their SoH trajectories remain relatively smooth. This suggests that the higher current produces a stronger operational penalty through polarisation.

#### Partial 5 °C Cooling Conditions

The cooling cases in Figure 5.5 show the clearest correspondence between cycling window behaviour and the early SoH divergence. T969 maintains a nearly constant window over the observed interval. After a small initial reduction, the final window is close to its BoL value. This agrees with the low capacity fade of T969 in Figure 5.2.

T963 shows a substantially different response under the same cooling condition. Its window decreases from approximately 44 to 32 percentage points by approximately 220 EFC. The contraction is again mainly caused by a downward shift of the upper boundary, with a smaller upward shift of the lower boundary at the final point.

T964 shows the strongest early contraction in the dataset. As shown in Figure 5.5b, its window decreases from approximately 55 to 33 percentage points within about 230 EFC. The lower boundary remains close to 13% SoC, while the upper boundary falls from approximately 67% to 45% SoC. This behaviour is consistent with the rapid capacity loss.

T991 shows a rapid initial contraction from approximately 38 to 28 percentage points, followed by limited further change. Since the SoH dataset is incomplete, a direct lifetime comparison cannot be made. The early contraction nevertheless indicates that the cooling configuration affected its accessible operating window from the beginning of the test.

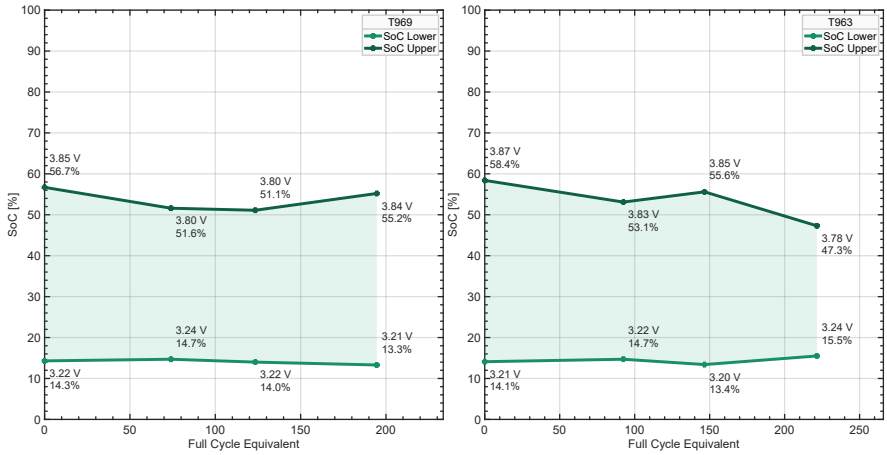


**(a)** Lower mantle cooling cells T969 and T963.

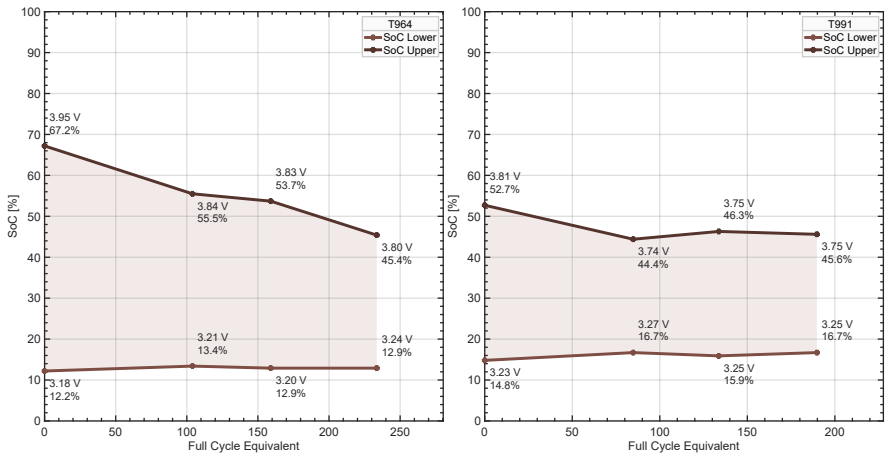


**(b)** Upper mantle cooling cells T964 and T991.

**Figure 5.5:** Evolution of the galvanostatic cycling SoC window for cells aged at 15 °C with partial lower or upper mantle cooling with 5 °C water.

## 5.4 ICI Resistance in Relation to the SoC Window

The ICI regression resistance, $R_{\mathrm{reg}}$, was compared at three selected health states to assess the contraction of the galvanostatic SoC window and its association with increasing polarisation. The labels BoL, MoL, and EoL in the figures denote the first, intermediate, and latest selected RPT, respectively. For cells that had not reached 80% SoH, the EoL label therefore represents the latest available measurement.

At fixed current, an increase in resistance adds to the terminal voltage response. During charge, this additional voltage rise can cause the upper voltage limit to be reached at a lower SoC. During discharge, the additional voltage drop can cause the lower voltage limit to be reached at a higher SoC.

The comparison is interpreted qualitatively because several cells show a BoL resistance that is substantially higher than the aged resistance. This is especially clear for T977 and is also visible for T961, T972, T974, T978, and T969. Such large apparent resistance reductions are not consistent with a credible ageing trend. The anomalously high BoL curves are therefore treated as unresolved measurement or conditioning offsets. Possible influences could be electrical contact resistance and voltage sensing.

For T961 in Figure 5.6a, the EoL resistance is approximately 3–7 mΩ larger than at MoL over much of the active SoC range. This late increase occurs together with the gradual upper boundary shift in Figure 5.3a and the late SoH knee in Figure 5.2. However, the BoL resistance is already as high as, or higher than, the latest curve. The result indicates a late change relative to MoL.

T971 shows a smaller and more consistent increase. The latest curve is approximately 1–1.5 mΩ above the MoL curve at high SoC, while the curves remain close at low SoC. This agrees with the upper SoC boundary decreasing from approximately 74% to 65%, while the lower boundary remains nearly unchanged. The high SoC resistance increase may therefore contribute to the earlier window contraction of T971, but it does not fully explain the difference in lifetime between T961 and T971.

T972 shows the clearest late stage change among the 15 °C non cooled cells. Within its cycling range, $R_{\mathrm{reg}}$ increases by about 3–4 mΩ from MoL to the latest state. This occurs during the same part of life in which the upper SoC boundary falls from approximately 55% to 37% and the SoH trajectory develops a knee. The results are consistent with increasing polarisation con-

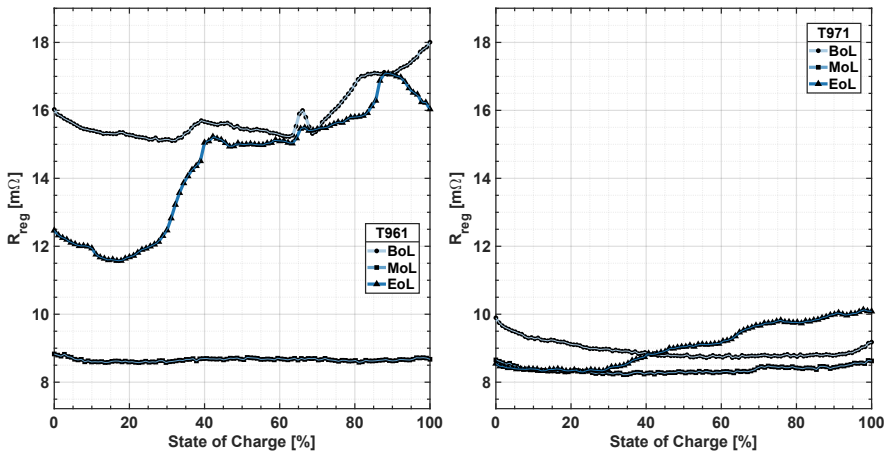


**(a)** 15 °C reference cells T961 and T971.

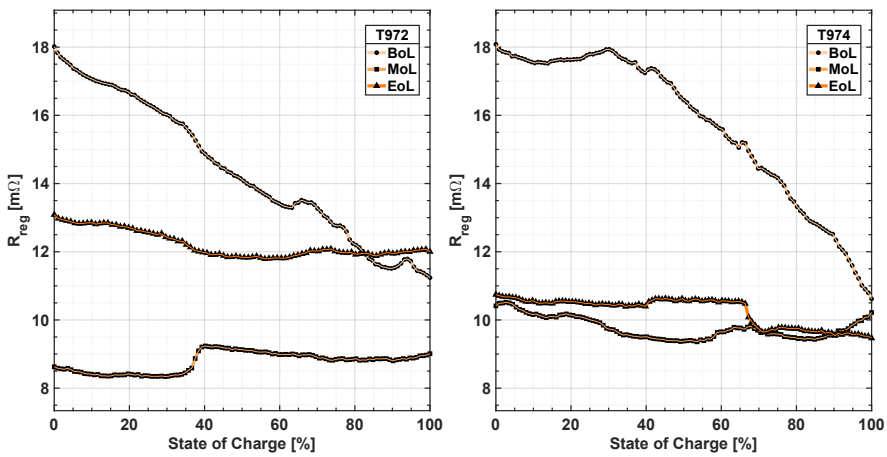


**(b)** 15 °C higher-rate cells T972 and T974.

**Figure 5.6:** ICI regression resistance as a function of SoC at selected BoL, MoL, and latest available states for cells aged at 15 °C under the reference and higher rate conditions.

tributing to the rapid late contraction of the cycling window.

For T974, the MoL and latest curves remain close through most of the active SoC range. The measured $R_{\mathrm{reg}}$ change is too small to explain the temporary closure and reopening of the SoC window in Figure 5.3b. Variable contact resistance or atypical cell quality remains a possible explanation.

For T965 in Figure 5.7a, all three curves remain within approximately 8–10 mΩ, and the difference between MoL and the latest state is generally below 1 mΩ.

The T977 BoL curve is approximately 32–43 mΩ, compared with approximately 6–10 mΩ for the aged curves. This apparent decrease is too large to represent a credible ageing trend and the T977 resistance evolution cannot be interpreted quantitatively from the present data. T978 shows little difference between the MoL and latest curves, which remain close to 10–11 mΩ.

T983 provides a clearer relation. Within the active SoC range, the latest resistance is approximately 3–5 mΩ above BoL. This increase occurs together with the upper boundary decreasing from approximately 66% to 47% SoC. The resistance growth is consistent with the progressive loss of accessible cycling window. The SoH trajectory remains smooth, showing that resistance growth and window contraction can develop without an abrupt capacity knee.

For T969 in Figure 5.8a, the MoL and latest curves remain close within the SoC range used during ageing. The latest resistance increases mainly above approximately 70% SoC, which is outside its upper cycling boundary. This agrees with the nearly stable SoC window and low capacity fade of T969. The much higher BoL curve is considered unresolved since the cause of it being high is not clear.

T963 shows an early increase of approximately 3–4 mΩ from BoL to the aged states within the active SoC range. This increase is consistent with the upper boundary decreasing from approximately 58% to 47% SoC and with the early SoH acceleration. The MoL curve is slightly higher than the latest curve over part of the range, so the resistance evolution is not monotonic. A clear conclusion is difficult to make from this data alone.

T964 shows a similar early increase of approximately 3–4 mΩ. Over the same period, its upper SoC boundary decreases from approximately 67% to 45%. T964 provides one of the clearest links between increased $R_{\mathrm{reg}}$, contraction of the cycling window, and early capacity loss. The slightly lower EoL resistance compared with MoL again shows that the resistance is an associated

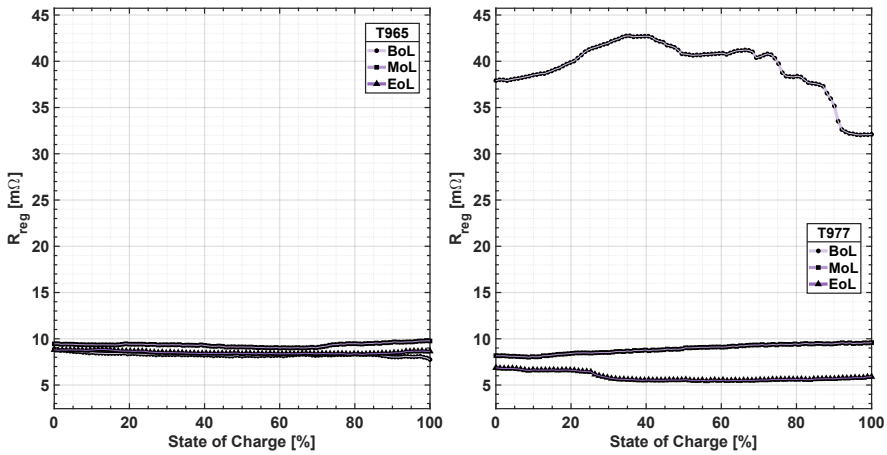


**(a)** 25 °C reference cells T965 and T977.

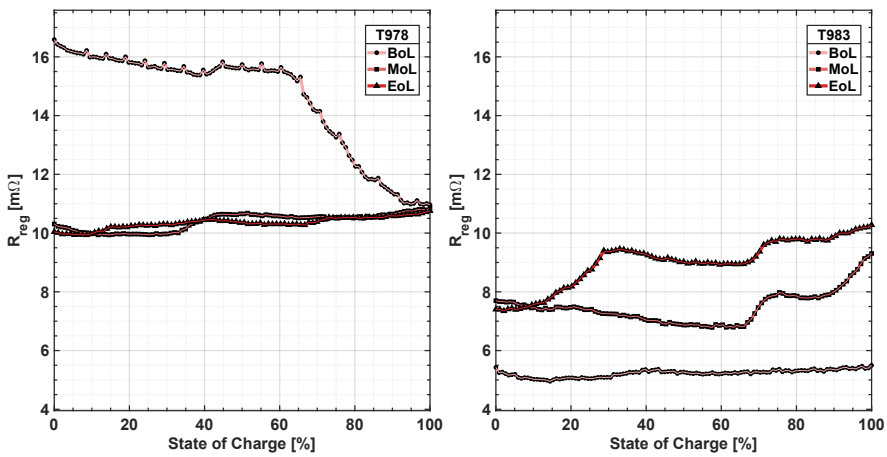


**(b)** 25 °C higher-rate cells T978 and T983.

**Figure 5.7:** ICI regression resistance as a function of SoC at selected BoL, MoL, and latest available states for cells aged at 25 °C under the reference and higher rate conditions.

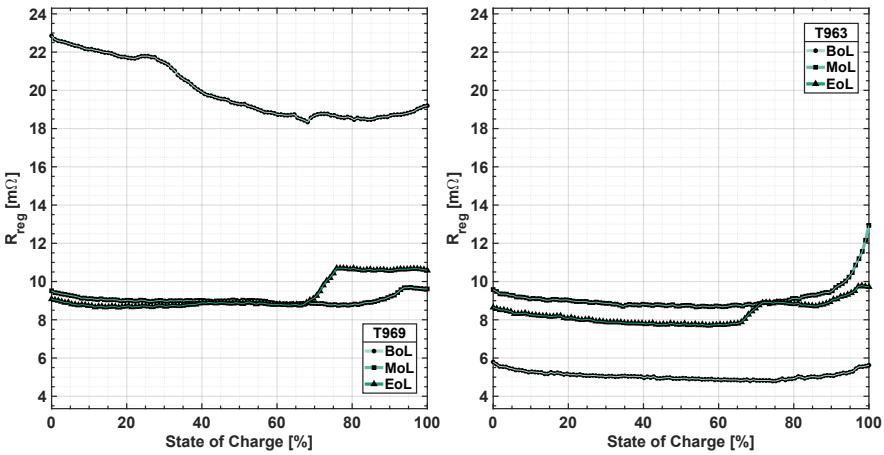


**(a)** Lower partial cooling cells T969 and T963.

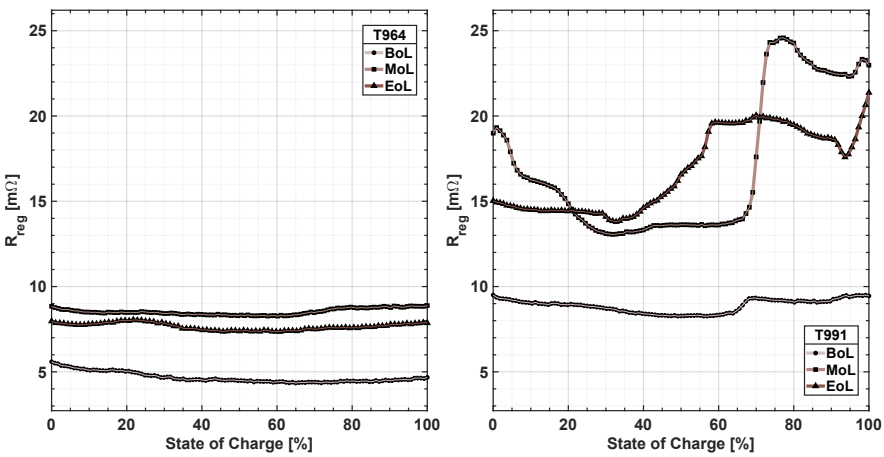


**(b)** Upper partial-cooling cells T964 and T991.

**Figure 5.8:** ICI regression resistance as a function of SoC at selected BoL, MoL, and latest available states for cells aged at 15 °C with partial lower or upper cooling using 5 °C coolant.

indicator rather than the only variable controlling the later SoH decline.

For T991, the aged resistance is approximately 5–10 mΩ higher than BoL over much of its active SoC range. This agrees with the early contraction of its cycling window. However, the SoH data is incomplete.

The clearest agreement between resistance growth and SoC window contraction is observed for T963, T964, T983, and T991. T972 also shows a clear late increase from MoL to the latest state, while T971 shows a smaller increase concentrated at high SoC. In these cells, increasing $R_{\mathrm{reg}}$ seems to provide a contribution to the downward shift of the upper cycling boundary.

The relation is weak or absent for T965, T969, T974, and T978. T977 cannot be interpreted quantitatively because of the anomalously high BoL curve, and T961 only shows a clear increase relative to MoL rather than from BoL. The present dataset therefore does not support a universal monotonic relation between $R_{\mathrm{reg}}$, SoC window contraction, and SoH fade.

The SoC window and RPT SoH also describe different aspects of ageing. Increasing resistance can directly reduce the capacity accessible during voltage limited galvanostatic cycling. In contrast, a knee in low rate RPT capacity indicates that additional irreversible degradation has developed. Where resistance growth, window contraction, and SoH acceleration occur together, as for T972, T963, and T964, they should be described as coupled indicators of the developing ageing state. The data do not show that resistance growth alone causes the capacity knee.

## 5.5 Thermal Profiles

Three surface temperature sensors were attached along the cell axis, one at the bottom, one at the middle, and one at the top close to the tab region. For each sensor, the marker in Figures 5.9–5.11 represents the average temperature during the selected lifecycle. The lower and upper lines represent the average minimum and average maximum temperature, respectively, during cycling. The lines describe the typical temperature swing during the cycling.

### 15 °C Reference and Higher Rate Conditions

The 15 °C reference cells in Figure 5.9a show comparatively small axial temperature differences. During the first lifecycle, the three average sensor temperatures differ by less than approximately 1 °C for both cells. In the latest lifecycle, the difference increases to about 2 °C, with the top of T961 and the middle of T971 being the warmest measured locations.

The average temperatures of both cells decrease slightly with ageing. T961 decreases from approximately 25 °C during the first lifecycle to approximately 22–24 °C during the latest lifecycle. T971 decreases from approximately 24 °C to approximately 21–23 °C. The average maximum temperatures also decrease. This cooling trend occurs despite the late SoH knees of T961 and T971 in Figure 5.2. It should therefore not be interpreted as a reduction in cell resistance or heat generation alone. As the cells age, the accessible SoC window contracts and less charge is transferred during each voltage limited ageing cycle. The shorter effective cycling interval can reduce the average and maximum temperature even when polarisation has increased.

The higher rate cells in Figure 5.9b show similar behaviour. T972 decreases from approximately 25–27 °C during the first lifecycle to approximately 23–24 °C during the latest lifecycle. Its axial average gradient remains small, at approximately 2 °C or less. T972 simultaneously shows a late increase in $R_{\mathrm{reg}}$, a strong contraction of the SoC window, and a capacity knee. The lower temperature in the latest lifecycle is therefore likely dominated by the smaaller cycling window and reduced energy throughput, rather than by lower electrochemical losses.

T974 also becomes cooler during the latest lifecycle. The bottom average temperature decreases to approximately 21 °C, while the top and middle remain near 23–24 °C. The axial average gradient consequently increases to

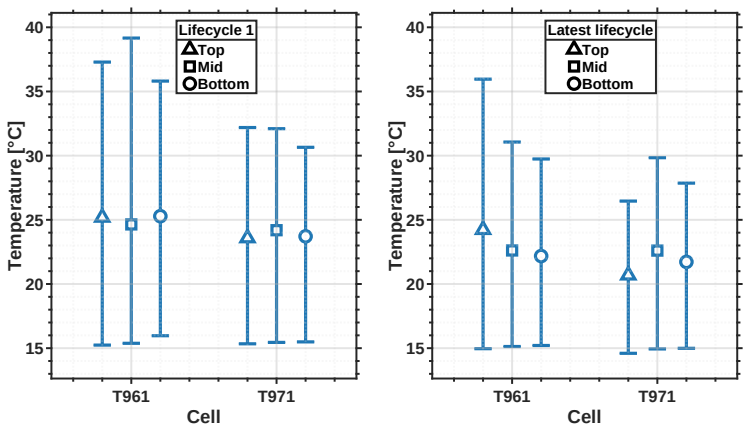


**(a)** 15 °C reference cells T961 and T971.

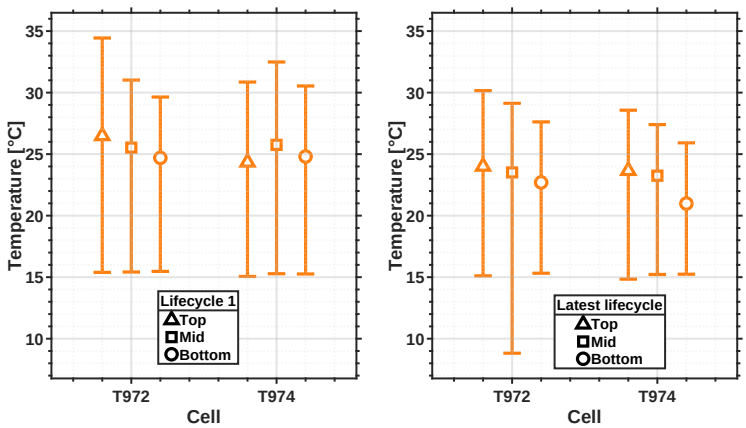


**(b)** 15 °C higher-rate cells T972 and T974.

**Figure 5.9:** Average top, middle, and bottom surface temperatures during the first and latest available lifecycles for cells aged at 15 °C. The lines show the average minimum and average maximum temperature during cycling.

approximately 3 °C.

### 25 °C Reference and Higher Rate Conditions

The 25 °C reference cells in Figure 5.10a operate at average surface temperatures of approximately 38–43 °C. T965 changes only slightly between the first and latest lifecycles, and its axial average gradient remains close to 1–2 °C. T977 shows a more noticeable increase at the top sensor, from approximately 38 °C to approximately 41 °C, while the middle and bottom temperatures change less. Its latest axial gradient is therefore approximately 2 °C.

The higher rate cells in Figure 5.10b show the largest lifetime related temperature increase in the dataset. During the first lifecycle, the three average temperatures are approximately 44–46 °C. During the latest lifecycle, they increase to approximately 47–51 °C, and the maximum top temperature approaches 58–59 °C. The increase is strongest at the top sensor close to the tab region. The gradient temperature difference grows from approximately 1–2 °C during the first lifecycle to approximately 3–4 °C during the latest lifecycle.

T978 shows a similar thermal increase even though its selected $R_{\mathrm{reg}}$ curves do not show a clear monotonic rise. This demonstrates that the thermal response contains contributions that are not fully represented by the ICI regression resistance metric. The temperature also depends on cycle duration, and heat transfer conditions.

### Artificially Induced Gradients Under Partial Cooling

The partial cooling cases in Figure 5.11 produce substantially larger axial surface temperature gradients than the uniformly conditioned cells. The two cooling configurations produce opposite axial temperature distributions. For the lower partial cooling cells, T969 and T963, the bottom sensor is the coldest measured location and the top sensor is the warmest. For the upper partial cooling cells, T964 and T991, the top sensor is the coldest and the bottom sensor is the warmest. The middle sensor generally has an intermediate temperature.

The resulting average axial gradient is approximately 5–8 °C, compared with generally less than 4 °C in the non-partially cooled cells. For the lower partial cooling cells, the measured surface temperature increases from the bottom toward the top of the cell. For the upper partial cooling cells, the

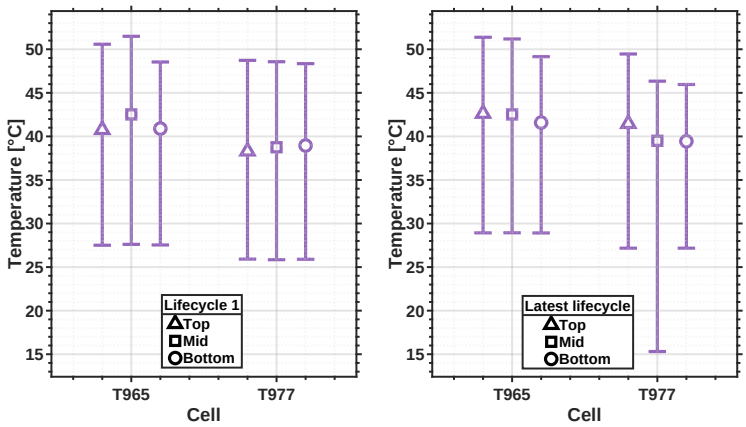


**(a)** 25 °C reference cells T965 and T977.

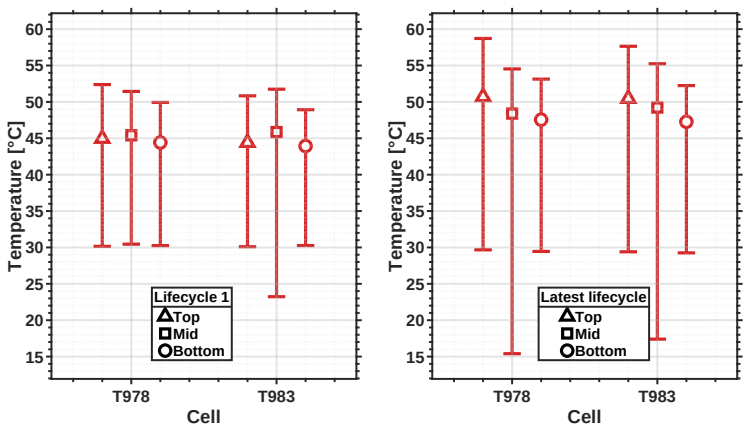


**(b)** 25 °C higher rate cells T978 and T983.

**Figure 5.10:** Average top, middle, and bottom surface temperatures during the first and latest available lifecycles for cells aged at 25 °C. The lines show the average minimum and average maximum temperature during cycling.

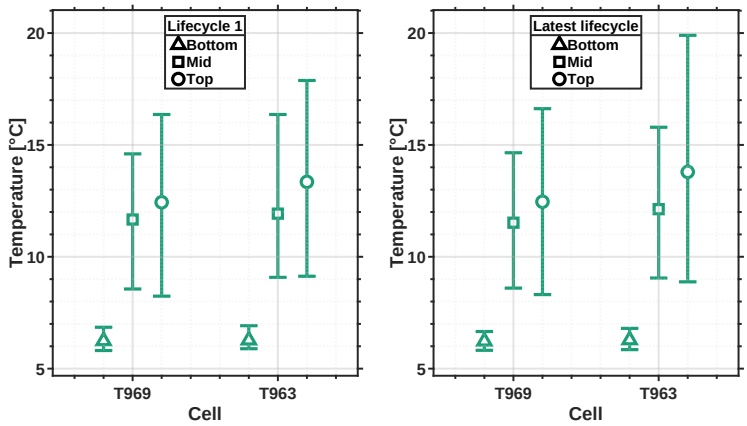


**(a)** Lower partial cooling cells T969 and T963.

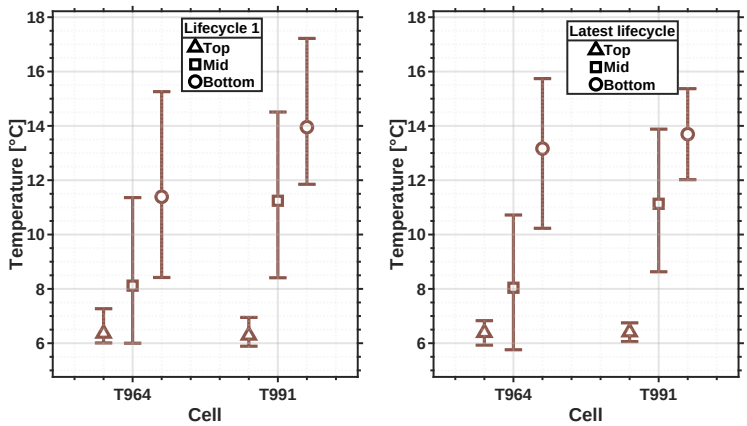


**(b)** Upper partial cooling cells T964 and T991.

**Figure 5.11:** Average top, middle, and bottom surface temperatures during the first and latest available lifecycles for cells aged with partial 5 °C cooling. The whiskers show the average minimum and average maximum temperature during cycling.

measured surface temperature increases from the top toward the bottom.

The spatial difference is larger during the hottest part of the cycle. For T963 in the latest lifecycle, the top sensor reaches an average maximum temperature close to 20 °C, while the bottom sensor remains below 7 °C. The corresponding peak top to bottom difference is therefore approximately 13 °C. The peak differences are approximately 9–10 °C for T969 and approximately 9 °C for T964 and T991. Partial cooling therefore creates a strong and persistent temperature gradient across the cell height.

T969 shows little change between the first and latest lifecycles. Its average top to bottom gradient remains approximately 6 °C. The bottom average temperature remains near 6 °C, while the top remains near 12.5 °C. This stable thermal profile is consistent with its nearly unchanged SoC window and low capacity fade over the observed interval.

T963 experiences a similar spatial temperature ordering, but its warm end becomes hotter with ageing. The average top to bottom gradient increases slightly from approximately 7.2 °C during the first lifecycle to approximately 7.6 °C during the latest lifecycle. The top average temperature increases from approximately 13.4 °C to approximately 14 °C, while its average maximum increases from approximately 18 °C to approximately 20 °C. The bottom temperature remains almost unchanged. The increased thermal non-uniformity is therefore mainly caused by heating at the top of the cell.

For the upper partial cooling cells, T964 shows the clearest lifetime-related change. Its average top to bottom gradient increases from approximately 5 °C to approximately 7 °C. The bottom average temperature rises from approximately 11.5 °C to approximately 13 °C, while the top remains close to 6 °C. This increase in thermal non-uniformity occurs together with the strongest early SoC window contraction and the earliest SoH knee in the dataset.

T991 maintains an average top to bottom gradient of approximately 7–8 °C, with little change between the two lifecycles. The top remains close to 6 °C, while the bottom remains close to 14 °C. Its incomplete SoH history prevents a direct conclusion about the long term effects.

**Table 5.2:** Approximate average axial surface-temperature gradients, calculated from the three marker temperatures in Figures 5.9–5.11.

| Cell | $\Delta T_{\mathrm{ax,avg,BoL}}$ | $\Delta T_{\mathrm{ax,avg,EoL}}$ |
|---|---|---|
| T961 | $\sim 0.6\,^{\circ}\mathrm{C}$ | $\sim 2.1\,^{\circ}\mathrm{C}$ |
| T971 | $\sim 0.5\,^{\circ}\mathrm{C}$ | $\sim 1.9\,^{\circ}\mathrm{C}$ |
| T972 | $\sim 1.9\,^{\circ}\mathrm{C}$ | $\sim 1.5\,^{\circ}\mathrm{C}$ |
| T974 | $\sim 1.3\,^{\circ}\mathrm{C}$ | $\sim 2.9\,^{\circ}\mathrm{C}$ |
| T965 | $\sim 1.5\,^{\circ}\mathrm{C}$ | $\sim 1.0\,^{\circ}\mathrm{C}$ |
| T977 | $\sim 0.7\,^{\circ}\mathrm{C}$ | $\sim 2.0\,^{\circ}\mathrm{C}$ |
| T978 | $\sim 1.1\,^{\circ}\mathrm{C}$ | $\sim 3.2\,^{\circ}\mathrm{C}$ |
| T983 | $\sim 2.0\,^{\circ}\mathrm{C}$ | $\sim 3.6\,^{\circ}\mathrm{C}$ |
| T969 | $\sim 6.2\,^{\circ}\mathrm{C}$ | $\sim 6.2\,^{\circ}\mathrm{C}$ |
| T963 | $\sim 7.2\,^{\circ}\mathrm{C}$ | $\sim 7.6\,^{\circ}\mathrm{C}$ |
| T964 | $\sim 5.1\,^{\circ}\mathrm{C}$ | $\sim 6.7\,^{\circ}\mathrm{C}$ |
| T991 | $\sim 7.7\,^{\circ}\mathrm{C}$ | $\sim 7.3\,^{\circ}\mathrm{C}$ |

## 5.6 CT Observations of Internal Structural

CT imaging was used to examine the internal jelly roll structure of selected cells. The representative BoL cross section in Figure 5.12 shows a largely circular central cavity and a regularly wound electrode structure. Local deformation is visible near the electrode extremities, including an apparent deformation of the anode.

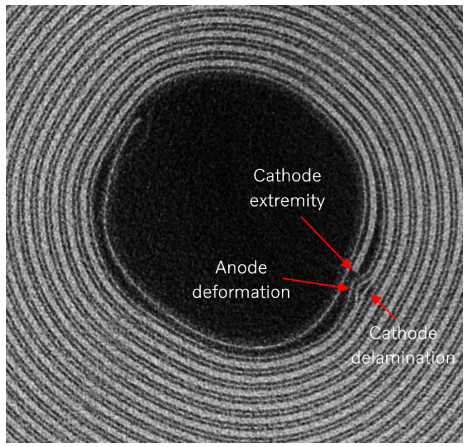


**Figure 5.12:** Representative CT image at BoL, showing the central cavity and the innermost jelly roll layers. The indicated regions show local anode deformation.

At EoL, cell T977 shows a pronounced loss of the original circular core geometry, as shown in Figure 5.13. The innermost jelly roll layers have displaced inward toward the central cavity. This structural change is described here as an apparent core collapse.

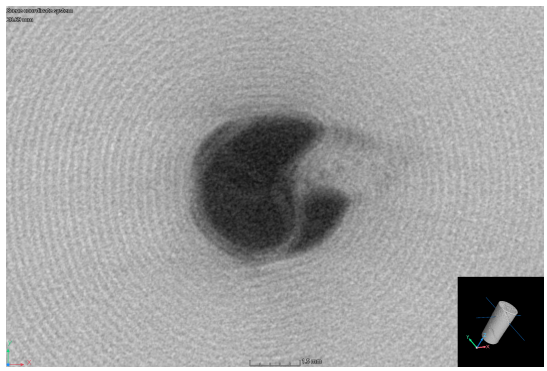

**Figure 5.13:** CT image of cell T977 at EoL, showing inward deformation of the innermost jelly roll layers and apparent core collapse.

The origin of the deformation cannot be determined from the CT image alone. Possible contributing factors include accumulated mechanical stress from electrode expansion and contraction, non-uniform internal pressure, local winding defects, and spatial differences in temperature. These explanations remain hypotheses and require further post mortem analysis.

The observation is nevertheless relevant because deformation of the inner jelly roll layers may alter local compression, porosity, ionic transport, and electrical contact. Such changes could contribute to heterogeneous ageing. However, the present images do not establish that the apparent core collapse caused the measured capacity fade. T977 also showed a comparatively smooth SoH trajectory rather than a sharp capacity knee, indicating that substantial structural deformation may develop without an abrupt feature in the capacity retention curve.

# CHAPTER 6

# Conclusions and Future Work

This thesis developed and evaluated methods for studying electrochemical and thermal non-uniformity in lithium ion cells. Laboratory Si–Gr cells were used to investigate material related voltage signatures, while prototype 4695 cells were used to study lifetime behaviour under different current, temperature, and cooling conditions. The main methodological conclusion is that capacity alone gives an incomplete description of ageing. The combined use of slow cycle voltage data, galvanostatic SoC window reconstruction, ICI resistance, surface temperature measurements, and CT imaging provided a more complete view of cell behaviour.

For the Si–Gr cells, the C/20 voltage hysteresis increased systematically with nominal $SiO_x$ content and was most clearly separated at low SoC. The 4695 cell showed the closest agreement with the nominal 10% $SiO_x$ reference, although this cannot be used to determine its exact silicon content. Ageing also depended strongly on the applied SoC window. The 15% Si–Gr cells cycled over 0–50% SoC reached approximately 80% SoH after 290 EFC, compared with about 350 EFC for the full 0–100% window. The 50–100% cells retained approximately 85% SoH after 360 EFC, while the graphite reference cells retained approximately 94–96% SoH after 400 EFC. The results show

that the low SoC region was most demanding for the investigated Si–Gr cells.

The 4695 cells showed both smooth capacity fade and pronounced knees. The ageing coordinate required to approach 80% SoH ranged from approximately 350 to 1030 EFC. Large differences were also observed between nominal replicates. T961 reached the 80% region about 250 EFC later than T971, while the difference between T965 and T977 was about 150 EFC. These differences were comparable to several apparent differences between test conditions. The present dataset therefore supports conclusions about individual trajectories, but not a robust ranking of temperature or current conditions.

For most cells, the galvanostatic SoC window contracted mainly because the upper SoC boundary moved downward. In several cases, this contraction developed during the same period as resistance growth and accelerated capacity fade. T972, T963, and T964 showed the clearest combined changes. However, the relation was not consistent for all cells, and several BoL resistance curves contained unexplained offsets. The SoC window and ICI measurements are therefore useful ageing indicators, but the present data do not show that resistance growth alone caused the observed knees.

The partial cooling system successfully created a persistent axial surface temperature gradient in the 4695 cells. The average measured gradient increased from generally below 4 °C without partial cooling to approximately 5–8 °C, with peak differences up to approximately 13 °C. T963 and T964 showed early SoC window contraction, resistance growth, and capacity loss, while T969 retained about 98% SoH after 330 EFC despite a similar imposed gradient. The results therefore show that strong thermal non-uniformity can coexist with early degradation, but do not prove that the gradient alone caused it or that one cooling position was more harmful than the other.

The thermal profiles also showed that average temperature must be interpreted together with current, cycle duration, and accessible SoC window. Several 15 °C cells became cooler during later cycling because the usable SoC window had decreased. In contrast, the 25 °C cells cycled at 0.8C/0.8C increased from average surface temperatures of approximately 44–46 °C to 47–51 °C, with maximum values close to 58–59 °C. CT imaging also revealed an apparent core collapse in T977, but its cause and effect on ageing has not been established.

The main limitations of the ageing experiment were the use of early prototype cells, only two cells per condition, incomplete test duration, uncertainties

with regards to electrical contact resistance, and high sensitivity in the PT100 contact to the cell surface. The methods are best regarded as demonstrated and useful, but not yet fully validated for quantitative comparison between test conditions.

## 6.1 Future Work

Future work should use a new batch of cells with higher manufacturing maturity and improved quality consistency. At least three cells should be included per test condition to separate protocol effects from cell variation. Electrical contact resistance, PT100 position, and sensor contact should be standardised and verified before long term testing to improve data quality.

A more focused test matrix should be used. Ageing should be performed with CCCV charging rather than purely galvanostatic charging so that the cells are returned to a consistent upper voltage and a more comparable SoC window throughout life. For the partial cooling tests, increasing the coolant temperature from 5 °C to approximately 15 °C would provide a more realistic boundary condition and simplify comparison with the reference cases.

Half-cell data should be analysed to separate changes in the positive and negative electrodes and to improve interpretation of the full cell ageing trends. This should be combined with further electrochemical analysis. Extensive teardown analysis should then be used to relate the electrical and thermal observations to local material changes and how degradation distributes within the cell to better understand heterogeneous effects.

Finally, all cells a the new batch should ideally be CT scanned at BoL and EoL. This would allow the occurrence and development of core collapse to be compared across the complete test matrix and related to capacity fade, resistance growth, thermal history, and cooling condition.

# References


[1] *Naturvårdsverket - Sweden's Climate Act and Climate Policy Framework*, en. Accessed: Jan. 26, 2026. [Online]. Available: https://www.naturvardsverket.se/en/international/swedish-environmental-work/swedens-climate-act-and-climate-policy-framework/.

[2] *Together we create the future electromobility • Swedish Electromobility Centre*, en-US. Accessed: Jan. 26, 2026. [Online]. Available: https://emobilitycentre.se/.

[3] M. Klett et al., "Non-uniform aging of cycled commercial LiFePO4//graphite cylindrical cells revealed by *post-mortem* analysis," *Journal of Power Sources*, vol. 257, pp. 126–137, Jul. 2014, ISSN: 0378-7753. Accessed: Jan. 28, 2026.

[4] M. Klett et al., "Uneven Film Formation across Depth of Porous Graphite Electrodes in Cycled Commercial Li-Ion Batteries," *The Journal of Physical Chemistry C*, vol. 119, no. 1, pp. 90–100, Jan. 2015, ISSN: 1932-7447. Accessed: Jan. 28, 2026.

[5] S. Li, C. Zhang, Y. Zhao, G. J. Offer, and M. Marinescu, "Effect of thermal gradients on inhomogeneous degradation in lithium-ion batteries," en, *Communications Engineering*, vol. 2, no. 1, p. 74, Oct. 2023, ISSN: 2731-3395. Accessed: Jan. 28, 2026.

[6] S. Li, M. W. Marzook, C. Zhang, G. J. Offer, and M. Marinescu, "How to enable large format 4680 cylindrical lithium-ion batteries," *Applied En-*

*ergy*, vol. 349, p. 121 548, Nov. 2023, ISSN: 0306-2619. Accessed: Nov. 16, 2025.

[7] A. S. Mussa et al., "Fast-charging effects on ageing for energy-optimized automotive LiNi1/3Mn1/3Co1/3O2/graphite prismatic lithium-ion cells," *Journal of Power Sources*, vol. 422, pp. 175–184, May 2019, ISSN: 0378-7753. Accessed: Jan. 29, 2026.

[8] P. Svens, A. J. Smith, J. Groot, M. J. Lacey, G. Lindbergh, and R. W. Lindström, "Evaluating Performance and Cycle Life Improvements in the Latest Generations of Prismatic Lithium-Ion Batteries," *IEEE Transactions on Transportation Electrification*, vol. 8, no. 3, pp. 3696–3706, Sep. 2022, ISSN: 2332-7782. Accessed: Jan. 29, 2026.

[9] A. S. Mussa, G. Lindbergh, M. Klett, P. Gudmundson, P. Svens, and R. W. Lindström, "Inhomogeneous active layer contact loss in a cycled prismatic lithium-ion cell caused by the jelly-roll curvature," *Journal of Energy Storage*, vol. 20, pp. 213–217, Dec. 2018, ISSN: 2352-152X. Accessed: Jan. 29, 2026.

[10] T. Waldmann et al., "Efficient Workflows for Detecting Li Depositions in Lithium-Ion Batteries," en, *Journal of The Electrochemical Society*, vol. 171, no. 7, p. 070 526, Jul. 2024, ISSN: 1945-7111. Accessed: Jan. 29, 2026.

[11] C. R. Birkl, M. R. Roberts, E. McTurk, P. G. Bruce, and D. A. Howey, "Degradation diagnostics for lithium ion cells," *Journal of Power Sources*, vol. 341, pp. 373–386, Feb. 2017, ISSN: 0378-7753. Accessed: Oct. 29, 2025.

[12] T. Waldmann et al., "Review—Post-Mortem Analysis of Aged Lithium-Ion Batteries: Disassembly Methodology and Physico-Chemical Analysis Techniques," en, *Journal of The Electrochemical Society*, vol. 163, no. 10, A2149, Aug. 2016, ISSN: 1945-7111. Accessed: Jul. 13, 2026.

[13] A. J. Smith, "Tools for characterizing performance degradation in lithium-ion batteries," eng, 2023. Accessed: Oct. 7, 2025.

[14] M. P. Bonkile et al., "Is silicon worth it? Modelling degradation in composite silicon–graphite lithium-ion battery electrodes," *Journal of Power Sources*, vol. 606, p. 234 256, Jun. 2024, ISSN: 0378-7753. Accessed: Oct. 8, 2025.

[15] Y. J. Choi et al., "Origins of Abrupt Capacity Degradation in Lithium-Ion Batteries with Silicon-Based Anodes," en, *Advanced Energy Materials*, vol. 15, no. 41, e02143, 2025, ISSN: 1614-6840.

[16] J. Jiang, X. Liu, and R. Yang, "Unveiling the multi-physical contributions in lithium plating for large cylindrical lithium-ion batteries during fast-charging," *Energy Storage Materials*, vol. 82, p. 104 560, Oct. 2025, ISSN: 2405-8297. Accessed: Oct. 14, 2025.

[17] S. D. Gelam, S. Maddipatla, C. Chicone, and M. Pecht, "Core collapse in cylindrical Li-ion batteries," *Journal of Power Sources*, vol. 623, p. 235 471, Dec. 2024, ISSN: 0378-7753. Accessed: Oct. 21, 2025.

[18] Z. Geng, T. Thiringer, and M. J. Lacey, "Intermittent Current Interruption Method for Commercial Lithium-Ion Batteries Aging Characterization," *IEEE Transactions on Transportation Electrification*, vol. 8, no. 2, pp. 2985–2995, Jun. 2022, ISSN: 2332-7782. Accessed: Oct. 29, 2025.

[19] N. Kirkaldy, M. A. Samieian, G. J. Offer, M. Marinescu, and Y. Patel, "Lithium-ion battery degradation: Comprehensive cycle ageing data and analysis for commercial 21700 cells," *Journal of Power Sources*, vol. 603, p. 234 185, May 2024, ISSN: 0378-7753. Accessed: Oct. 8, 2025.

[20] R. Wittman et al., "Characterization of Cycle-Aged Commercial NMC and NCA Lithium-ion Cells: I. Temperature-Dependent Degradation," en, *Journal of The Electrochemical Society*, vol. 170, no. 12, p. 120 538, Dec. 2023, ISSN: 1945-7111. Accessed: Oct. 8, 2025.

[21] F. Ringbeck, C. Rahe, G. Fuchs, and D. U. Sauer, "Identification of Lithium Plating in Lithium-Ion Batteries by Electrical and Optical Methods," en, *Journal of The Electrochemical Society*, vol. 167, no. 9, p. 090 536, May 2020, ISSN: 1945-7111. Accessed: Oct. 8, 2025.

[22] H. Ditler, T. Tegetmeyer-Kleine, G. Stahl, C. Rahe, and D. U. Sauer, "Lithium plating in commercial lithium-ion cells: An extensive study combining electrical methods with post-mortem analysis," *Journal of Energy Storage*, vol. 132, p. 117 706, Oct. 2025, ISSN: 2352-152X. Accessed: Oct. 8, 2025.

[23] L. Yin et al., "Implementing intermittent current interruption into Li-ion cell modelling for improved battery diagnostics," *Electrochimica Acta*, vol. 427, p. 140 888, Sep. 2022, ISSN: 0013-4686. Accessed: Oct. 29, 2025.

[24] Y.-C. Chien, H. Liu, A. S. Menon, W. R. Brant, D. Brandell, and M. J. Lacey, "Rapid determination of solid-state diffusion coefficients in Li-based batteries via intermittent current interruption method," en, *Nature Communications*, vol. 14, no. 1, p. 2289, Apr. 2023, ISSN: 2041-1723. Accessed: Oct. 29, 2025.

[25] *Welcome to EL-CELL – Electrochemical test equipment for battery research*, en-US. Accessed: Feb. 19, 2026. [Online]. Available: `https://www.el-cell.com/`.